



Experimentally characterising the temperature and rate dependent behaviour of unfilled, and glass microsphere filled, natural rubber

Akash R. Trivedi^a, Rory Whybrow^b, Alan H. Muhr^c, Clive R. Siviour^{a,*}

^a Department of Engineering Science, University of Oxford, Parks Road, Oxford, OX1 3PJ, Oxfordshire, United Kingdom

^b Department of Materials, University of Oxford, Parks Road, Oxford, OX1 3PH, Oxfordshire, United Kingdom

^c Tun Abdul Razak Research Centre, Brickendonbury, Hertford, SG13 8NL, Hertfordshire, United Kingdom

ABSTRACT

Low-impedance, elastomeric materials are widely used in engineering applications where they are subjected to impact loading leading to high strain rate deformation. The strong rate and temperature dependence that is exhibited by these polymers and their composites provides further motivation for a deeper understanding of this complex behaviour including the interaction between the matrix and filler materials. In this paper, unfilled and glass microsphere filled natural rubbers are used as model materials to better understand the behaviour of low-impedance particulate composites. These materials were characterised experimentally over a range of strain rates and temperatures. The effect of filler volume fraction and mean particle diameter on the rate and temperature dependence of the overall mechanical response was also investigated, as well as damage evolution based on post-deformation analysis of interrupted compression experiments. In this paper, experimental insights and data are presented and discussed, which will influence future constitutive modelling efforts.

1. Introduction

Particulate composites are extensively used in engineering applications, ranging from concrete used as a basic construction material through to polymer bonded explosives (PBX) used in advanced weapons systems [1,2]. These two examples illustrate that the filler may act to strengthen the material, or the overall material may be designed to transport the filler itself. In many applications, the composites are used in systems where they can be subjected to impact loading, leading to high strain rate deformation, at a variety of temperatures. In systems where the matrix is a polymer, the overall mechanical response is likely to be highly rate and temperature dependent.

These dependencies can be studied through the use of model materials [3,4]. In this paper, unfilled and glass microsphere filled natural rubbers are used as generalised model materials to better understand the rate and temperature behaviour of low-impedance particulate composites. Filled and unfilled natural rubber (F/U-NR) are widely used in industrial applications such as seals, energy absorbers and vibration dampers, where they experience high strain rate deformation at various temperatures. As the strain rate of deformation increases or the temperature decreases, molecular motions in the polymer network become inhibited, leading to the strong rate and temperature sensitivity [5]. This consequently influences the mechanical response of the composite. This equivalence between rate and temperature has been investigated since

the 1970s, particularly in the context of modulus and yield stress, the latter for example in polymers including poly(methyl methacrylate) (PMMA) [6,7], PVC [8,9] and polycarbonate [10].

One of the most common methods for measuring the high strain rate properties of materials is the split-Hopkinson pressure bar (SHPB) [11, 12]. However, at high strain rates (above $c. 10 \text{ s}^{-1}$), experimental characterisation of the mechanical response of low-impedance materials becomes increasingly difficult as their low wave-speeds mean that the time taken to achieve static stress equilibrium during loading is similar to, or even greater than, the experimental duration [13]. Furthermore, for low-modulus materials, such as rubber, the experimental signals from which force is calculated are often too small to be measured accurately [14]. Researchers have overcome these challenges with the use of modifications to the SHPB including reduced cross-section bars [14], piezoelectric pressure transducers [15], and using ultra high-speed cameras to record images that allow full-field displacement and acceleration measurements, and negate the requirement for a static equilibrium [16].

The current paper provides a comprehensive experimental study characterising the temperature and rate dependent behaviour of unfilled, and glass microsphere filled, natural rubber. In addition to removing difficulties with stress equilibrium and instrumentation, a further advantage of focusing on lower strain rate experiments to understand the high rate behaviour (either through experimental

* Corresponding author.

E-mail address: Clive.Siviour@eng.ox.ac.uk (C.R. Siviour).

<https://doi.org/10.1016/j.polymer.2023.125773>

Received 10 May 2022; Received in revised form 1 February 2023; Accepted 6 February 2023

Available online 12 February 2023

0032-3861/© 2023 The Authors. Published by Elsevier Ltd. This is an open access article under the CC BY license (<http://creativecommons.org/licenses/by/4.0/>).

simulations [4,17,18] or calibrated models [19,20]) is that it opens up the possibility of using a wider range of diagnostic tools, e.g. Scanning Electron Microscope, X-ray tomography.

In previously published research, predictions of the mechanical response of PVC and plasticised PVC were made based on a novel modelling framework fully calibrated using quasi-static experiments, incorporating the time-temperature superposition (TTS) principle and the effects of adiabatic self-heating [19]. These predictions were shown to have excellent agreement with experiments from a previous study [21]. Here, progress is presented on extending this research to predict the high rate behaviour of particulate composites, with glass microsphere filled natural rubber (F-NR) as a model material. Filled and unfilled natural rubbers (U-NR) are softer, lower impedance materials than plasticised PVC, which prove even more challenging to characterise experimentally at high strain rates. F-NR is also an ideal model material to represent more complex PBX materials, making it a focus for this study.

2. Materials

Natural rubber latex extracted from the rubber tree, *Hevea brasiliensis*, is mainly formed of *cis*-1,4-polyisoprene. Its molecular structure can be seen in Fig. 1.

This latex forms the basis of the natural rubber (NR) used in this study. Plates of EDS 19 grade NR measuring 230 mm × 230 mm × 5 mm, for which the formulation can be found in Ref. [22], were manufactured at the Tun Abdul Razak Research Centre in Hertfordshire, UK. This was a conventional accelerated-sulphur vulcanizate containing no filler.

In order to produce particulate composites, glass microspheres were mixed into EDS 19 gum prior to curing. Two grades of spheres were used with an order of magnitude difference in the mean particle size; basic properties are shown in Table 1.

With each grade of spheres, two sets of particulate composites were produced, with a 5% and 50% volume filler fraction. By assuming a perfect mixture, the expected densities of the particulate composites can be estimated by using the rule of mixtures:

$$m = \rho V = m_f + m_m = \rho_f V_f + \rho_m V_m = \rho_f \phi_f V + \rho_m (1 - \phi_f) V \rho = \rho_f \phi_f + \rho_m (1 - \phi_f) \quad (1)$$

where the mass, m , is the product of the density, ρ , and the volume, V . The mass of the binary composite can be split into the contributions from the fibre, m_f , and the matrix, m_m . These in turn can also be represented by the product of their density and volume. By making use of the fact that the volume fractions, ϕ_f , are known for each composite, the volume of each constituent can be represented in terms of the overall volume of

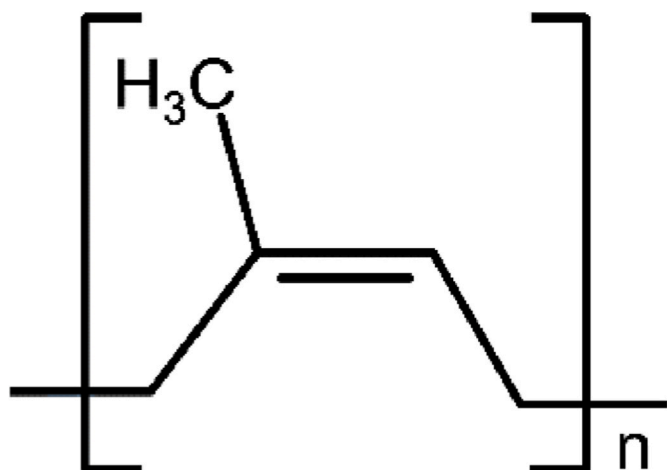


Fig. 1. Molecular structure for *cis*-1,4-polyisoprene.

Table 1

Material properties for U-NR and glass microsphere fillers.

Material	Density (kg m ⁻³)	Modulus (MPa)	Mean particle size (μm)	Particle range (μm)
EDS 19/U-NR	966	0.52 (23 °C, 2% strain, 0.1 Hz)	N/A	N/A
Spherglass 2429	1460 (bulk, untapped) 1570 (bulk, tapped)	69,000	70–100	53–106
Spherglass 5000	1280 (bulk, untapped) 1620 (bulk, tapped)	69,000	7–10	N/A

the composite, V . The density can then be estimated using Equation (1).

The densities of the filled composites are as follows: F-NR2, 996 kg m⁻³; F-NR3, 998 kg m⁻³; F-NR4, 1270 kg m⁻³; and F-NR5, 1290 kg m⁻³. In calculating these values, the so-called “tapped” densities of the microspheres as provided by the manufacturer were used, which are the slightly higher values obtained after mechanically tapping the container before measurement. The various F-NR grades are depicted diagrammatically in Fig. 2.

3. Specimen preparation

3.1. Uniaxial compression samples

Uniaxial compression experiments were all conducted on right circular cylindrical specimens of 5 mm length and diameter. This size was chosen based on geometry constraints in the high rate experiments, aimed at reducing inertial stress contributions [23].

The specimens were machined out of the manufactured plates using a bespoke cutter with a 5 mm diameter hole and 0.05 mm tapered cutting edge. A soap-water mix was used for cooling and lubrication to ensure there was not a substantial increase in temperature during machining, which might affect the polymer microstructure. A common alternative is to punch out samples using a suitable die; however, stresses during the punching process result in specimens resembling conical frustums, and as such, this method was not used.

3.2. Differential Scanning Calorimetry samples

Differential Scanning Calorimetry (DSC) specimens were required to be sealed inside a small aluminium pan with a nominal internal diameter of 5 mm and height of 1 mm. Since rubber samples of small thickness are challenging to machine, thin slivers from the compression specimens were cut manually using a scalpel. Each DSC sample required around 10 μg of the rubber material.

3.3. Dynamic Mechanical Analysis samples

Dynamic Mechanical Analysis (DMA) experiments were performed using a single cantilever configuration on specimens measuring 2 mm × 5 mm × 40 mm, where the effective span length is 17.5 mm.

Initially, specimens measuring 5 mm × 10 mm × 40 mm were machined out of the manufactured plate, which had a thickness of 5 mm. Each large rectangular specimen was further trimmed manually down to a thickness of 2 mm with a scalpel, using a stiff metal plate as a guide.

4. Thermomechanical characterisation

4.1. Modulated Differential Scanning Calorimetry (MDSC)

DSC experiments measure the difference in heat flow between the sample and an inert reference as a function of time and temperature,

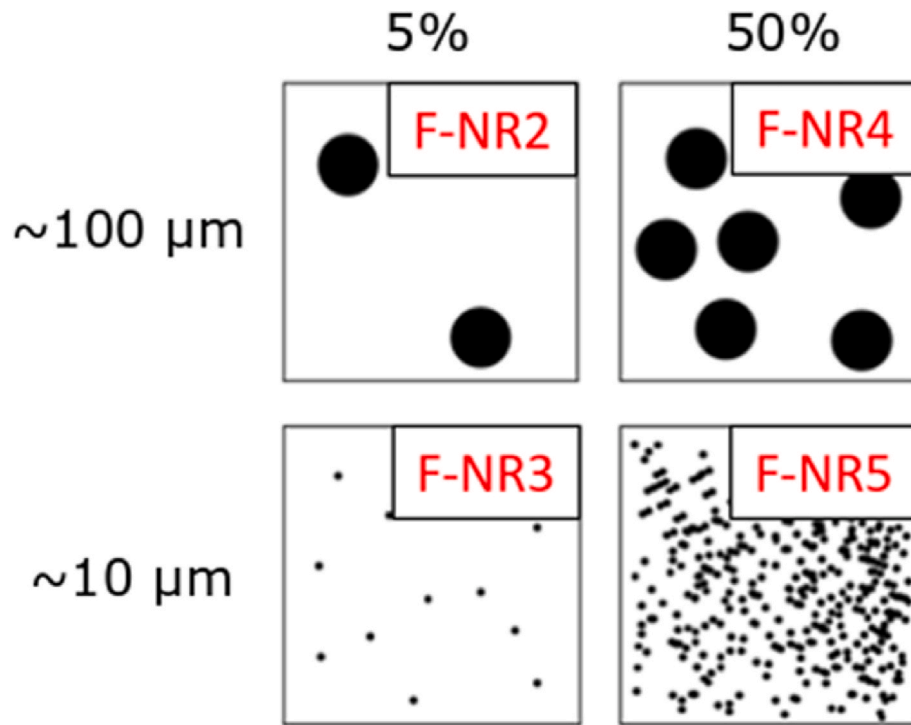


Fig. 2. Schematic diagram of the different grades of F-NR.

whilst they are both subjected to the same linear heating or cooling rate and environmental conditions. The difference in heat flow between the sample and reference can be used to identify and characterise thermal transitions of interest in the material. However, to separate complex transitions which may be overlapping, and to obtain the heat capacity, modulated DSC (MDSC) experiments were performed.

In MDSC experiments, a sinusoidal temperature oscillation is superposed onto the conventional temperature ramp and the difference in heat flow required to maintain this temperature profile is again monitored between the empty reference pan and the pan containing the specimen. MDSC experiments are also more sensitive than conventional DSC, allowing for weaker transitions to be resolved. Furthermore, they allow the separation of desired thermodynamic effects (such as the temperature dependent heat capacity) from undesired kinetic effects such as crystallisation or chemical reactions.

Three MDSC experiments on each material were performed over the temperature range $-90\text{ }^{\circ}\text{C}$ to $200\text{ }^{\circ}\text{C}$. This range ensures that the glass transition is covered, but also allows the elucidation of other transitions that may be present at typical temperatures encountered in this study. The experiments were conducted in accordance with the guidance in Ref. [24]: an underlying ramp of $3\text{ }^{\circ}\text{C min}^{-1}$; and a modulation with amplitude $0.5\text{ }^{\circ}\text{C}$, and period 60 s. The low amplitude provides good resolution of the measured heat flow, and the long period compensates for the low thermal diffusivity of neoprene rubber ($k \approx 10^{-7}\text{ m}^2\text{ s}^{-1}$ [25]).

4.1.1. Characterisation of self-heating

It was stated earlier that the modelling framework used to predict the high rate behaviour requires an understanding of the adiabatic self-heating. At higher rates, the specimen temperature increases as the heat cannot diffuse out on the time-scale of the experiment. This can then modify the mechanical response of the material. In order to find the temperature rise in the specimen due to this adiabatic self-heating, it is often assumed that all the mechanical work done on the specimen is converted to heat, so that the temperature rise can be calculated as:

$$\Delta T \approx \frac{1}{C_p(T)} \int_0^{\epsilon} \sigma(\epsilon) d\epsilon \quad (2)$$

where ρ is the density of the material, $C_p(T)$ is its temperature dependent heat capacity, and σ and ϵ are the true stress and strain in the sample. In order to use this equation, the temperature dependent heat capacity must first be obtained for each rubber grade using MDSC experiments.

The results of the MDSC experiments for U-NR are shown in Fig. 3. Three experiments were performed and the mean of the three experiments is plotted along with the individual results. Models are fitted to the mean data either side of the glass transition. Below T_g , an exponential description is fitted and above T_g , a linear fit is used.

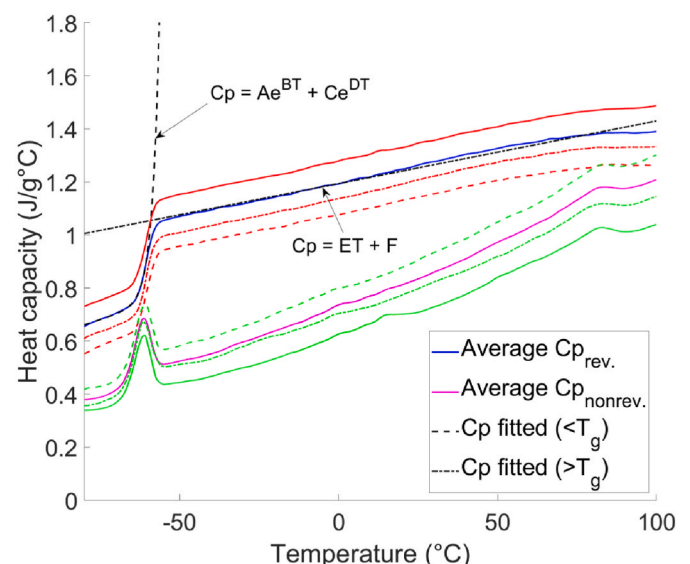


Fig. 3. MDSC results for U-NR with model fits either side of the T_g .

The MDSC results for the F-NRs are shown in Appendix A.1. The form of the results for the MDSC experiments on the particulate composites is the same as that of the U-NR, so the same exponential and linear models can be fit either side of their T_g , albeit with different parameters. Table 2 shows the parameters required for the model fits.

The three main thermal behaviours that can be extracted from these results are the calorimetric T_g of the material (calculated as the midpoint of the transition), the increase in heat capacity as the temperature increases through, and the temperature range of the glass transition.

To better aid comparison, the reversing C_p for each material is replotted in Fig. 4. The curves are shifted along the y-axis such that the ordinate at the onset of the glass transition has the same value for each curve. The addition of glass microspheres is observed to cause a reduction in the heat capacity change through the glass transition owing to there being less rubber in the material. Similar observations have been made with clay-polymer nanocomposites [26] and spherical silica-polymer nanocomposites [27].

The heat capacity results also show a small dependence on the particle size distribution. For the samples with smaller particle sizes (F-NR3/5), the heat capacity is slightly higher than that for the samples with larger particle sizes at the same filler volume fraction. This may be because there is a greater temperature dependence of interfacial energy for the composites with smaller particles as the surface area to volume ratio is larger.

There is a very slight broadening of the transition with increasing filler volume fraction. Three tangents can be drawn: at the T_g onset (c. -65°C); at the end of the glass transition (c. -55°C); and at the T_g (midpoint of the transition; can also be defined as where the magnitude of the slope is at its maximum). The lower point of intersection is where the T_g onset tangent meets the T_g tangent. The upper point of intersection is where the T_g end tangent meets the T_g tangent. The breadth of the transition is defined as difference in temperature between the upper and lower points of intersection. An illustration of this definition is shown in Fig. 5. For U-NR, $\Delta T = 4.2^\circ\text{C}$ and this increases to $\Delta T = 4.4^\circ\text{C}$ for the 5% F-NRs and $\Delta T = 5.1^\circ\text{C}$ for the 50% F-NRs. These values represent the mean value for the three experiments. This phenomenon is due to segmental dynamics becoming more heterogeneous as the mobility of polymer chains is greatly reduced in the interfacial region between the filler and matrix [28].

Based on these MDSC experiments, it is clear that the addition of glass microspheres at the levels used in this study does not influence the T_g : in each set of experiments, $T_g = -60^\circ\text{C}$. These T_g values are compared in the next section to the more sensitive DMA experiments.

4.2. Dynamic Mechanical Analysis (DMA)

In order to use the TTS principle, thermo-mechanical characterisation of each material was performed, using a TA Instruments Q800 DMA. The soft natural rubber can be challenging to characterise using this apparatus, as such, a bespoke methodology was developed in order to produce high quality results [in-press].

Fig. 6 shows the storage modulus, loss modulus and tan delta results for U-NR using this methodology. Although the data are shown as functions of temperature, they were obtained as isothermal frequency sweeps. In order to obtain data that can be used to perform TTS to a higher standard, isothermal frequency sweeps were performed, with

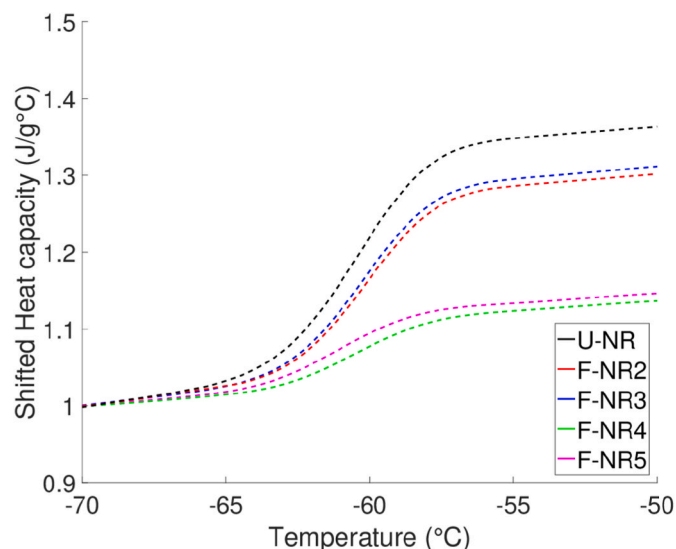


Fig. 4. Shifted MDSC results for all grades of NR to compare T_g , heat capacity rise and breadth of transition.

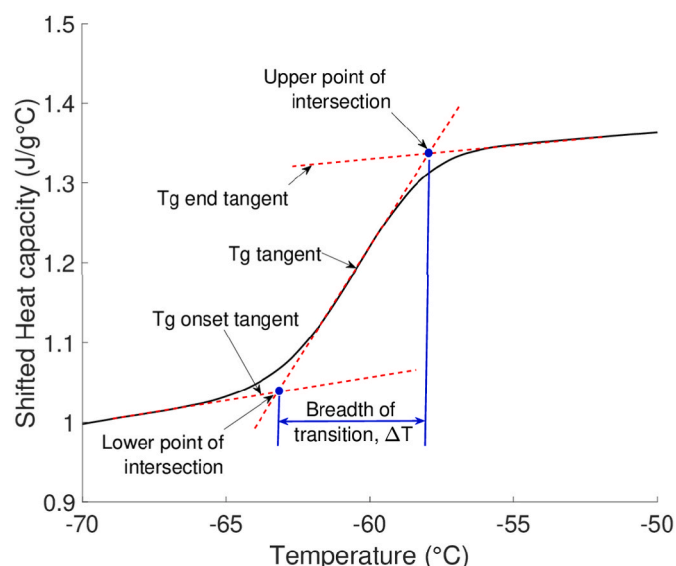


Fig. 5. Illustrating how the breadth of transition is defined.

seven frequencies at each temperature step, comprising three values per decade of frequency. A temperature range of -80°C to 40°C was used with 0.5°C steps inside the transition region (-80°C to -40°C), and 2.5°C steps outside. Owing to physical limitations of the cooling apparatus, which was not able to run continuously for the duration of the full temperature range, it was not feasible to perform DMA experiments from below T_g through to the desired reference temperature of 25°C in a single experiment. Therefore, two sets of experiments were performed and subsequently stitched together: one from -80°C to

Table 2

Parameters for the model fits to the MDSC results.

Material	A ($\text{J g}^{-1} \text{ } ^\circ\text{C}^{-1}$)	B ($^\circ\text{C}^{-1}$)	C ($\text{J g}^{-1} \text{ } ^\circ\text{C}^{-1}$)	D ($^\circ\text{C}^{-1}$)	E ($\text{J g}^{-1} \text{ } ^\circ\text{C}^{-2}$)	F ($\text{J g}^{-1} \text{ } ^\circ\text{C}^{-1}$)
U-NR	1.5×10^{11}	0.46	1.1	5.8×10^{-3}	2.4×10^{-3}	1.2
F-NR2	1.7×10^4	0.19	0.93	1.8×10^{-3}	2.5×10^{-3}	1.3
F-NR3	1.3×10^4	0.19	0.94	1.7×10^{-3}	2.7×10^{-3}	1.3
FNR4	1600	0.17	0.71	2.1×10^{-3}	1.9×10^{-3}	0.87
FNR5	1800	0.17	0.88	2.3×10^{-3}	1.8×10^{-3}	1.0

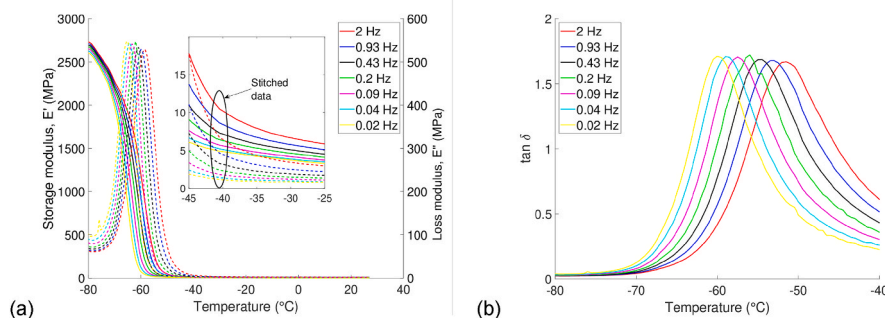


Fig. 6. DMA results for U-NR: (a) temperature dependent storage (solid line) and loss (dashed line) moduli, and (b) loss tangents.

−40 °C; and one from −50 °C to 40 °C. The stitching is shown in the inset of Fig. 6a.

Results for the DMA experiments on the 5% and 50% filled composites are found in Appendix A.2. The storage and loss moduli for both F-NR2 and F-NR3 are similar to those of U-NR, but the loss tangent peaks show a decreasing magnitude with increasing frequency. The addition of particles immobilises some of the polymer surrounding the filler, restricting the damping response [26]. This effect is magnified at higher frequencies, as the reduced time-scale over which the relaxations are allowed to occur leads to further restriction. The glassy storage modulus plateau is at approximately 7 GPa for both F-NR4 and F-NR5 — more than two times larger than those of U-NR, F-NR2 and F-NR3. There is also considerably less damping through the glass transition for the 50% filled composites: the loss tangent peaks are lower than those of the other three materials.

As with the MDSC experiments, the DMA experiments show that T_g does not differ between the U-NR and four F-NRs. Although an increase in frequency shifts the T_g higher, at the lowest frequencies interrogated, $T_g = -60$ °C.

4.3. Time-temperature superposition (TTS)

4.3.1. Master curves

Instead of plotting the modulus against temperature as in the previous section, it can be plotted against frequency instead, producing isotherms of the response. These are shown for U-NR in Fig. 7a.

By exploiting the time-temperature equivalence for the modulus and using a TTS shifting algorithm — in this case, the one described in Ref. [19] — the isotherms for U-NR shown in Fig. 7a can be shifted to construct the master curve, shown in Fig. 7b for a reference temperature of 25 °C. This process was also performed for the composites, to produce the set of master curves as shown in Fig. 8. Their isotherms can be found in Appendix A.3.

In these master curves, the low frequency plateau represents the

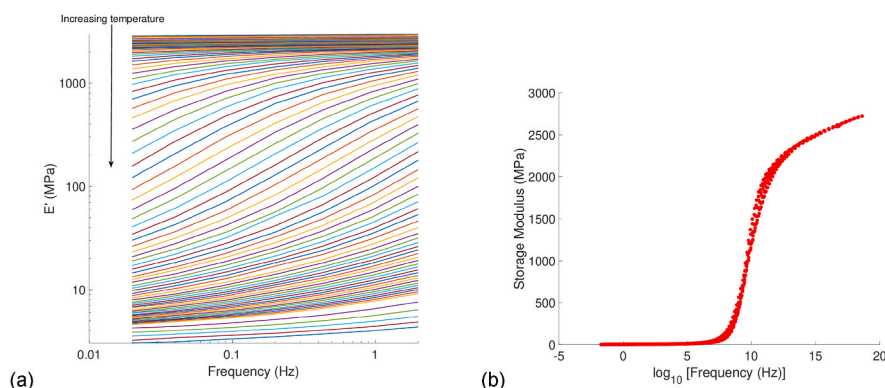


Fig. 7. (a) Isotherms from the DMA results for U-NR and (b) the master curve generated by shifting these at a reference temperature of 25 °C.

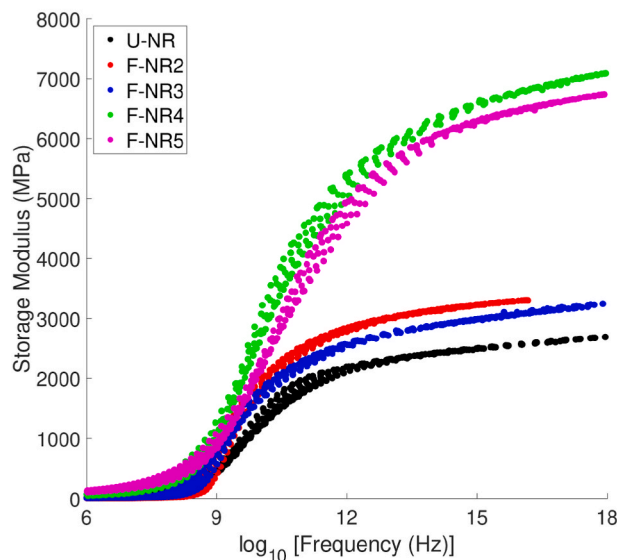


Fig. 8. Master curve for each material generated at a reference temperature of 25 °C.

long-term modulus, obtained from shifting the highest temperature isotherms. Conversely, the high frequency data, obtained from shifting the lowest temperature isotherms, approaches the instantaneous modulus. It is evident that the addition of fillers enhances the mechanical performance. A 5% volume fraction increases the high frequency modulus by an average of 24%. There is almost a threefold increase in the high frequency modulus when the filler volume fraction is increased to 50%.

4.3.2. Shift factor relationships

The temperature dependent shift factors for each material take an Arrhenius form [29] below T_g (shown for U-NR in Fig. 9a) and a WLF form [30] above T_g (Fig. 9b).

The shift factors for the filled rubbers have the same form of relationship as U-NR and are presented in Fig. 10. The slopes for the curves below T_g are almost the same, indicating they have the same activation energy. Table 3 quantifies this and details the constants used for the Arrhenius and WLF fits to the shift factor data.

4.3.3. Activation energies

It is possible to calculate the activation energy of the glass transition by analysing the glass transition temperature as a function of frequency, here identified as the peak of the loss tangent curves in Fig. 6 and 33–36. Furthermore, it is also possible to infer the value of the activation energy for the glass transition by considering the Arrhenius equation fitted to the shift factors below T_g .

The Arrhenius equation takes the form $A \exp(-Q/RT)$. Plotting the logarithm of the oscillation frequency against the reciprocal of the absolute temperature at which the loss tangent peak occurs, gives a curve of gradient $-Q/R$ where Q is the activation energy for the glass transition, and R is simply the gas constant. These plots are shown in Fig. 11 for the U-NR and the four particulate composites.

A comparison of the activation energies resulting from these two methods is in Table 4, along with the constants required to fit the Arrhenius expression to the loss tangent. Using the loss tangent consistently results in a higher value for the activation energy with a mean of 214 kJ mol^{-1} compared to the mean value of 152 kJ mol^{-1} obtained from the shift factors.

5. Uniaxial compression

5.1. Rate dependence

5.1.1. Experimental techniques

A full regime of compression experiments was performed at a variety of strain rates at temperatures around $22.5 \pm 2.5^\circ\text{C}$ on an Instron 5980 static testing machine ($10^{-3} - 10^{-1} \text{ s}^{-1}$), an in-house hydraulic press ($1-100 \text{ s}^{-1}$) and an SHPB (c. 10^3 s^{-1}), which was also used in a Direct Impact Hopkinson pressure bar (DIHPB) configuration to facilitate larger strains.

An Instron testing machine was instrumented with 2580 Series load cells and custom-built supports and loading anvils. Due to the low loads, compliance corrections were not necessary: preliminary experiments showed rig compliance to be negligible. However, in any case, an extensometer was attached to the anvils, close to the specimen and used to provide strain measurements and closed loop control. In this study, an Instron 2620 Series dynamic strain gauge extensometer with a 12.5 mm gauge length and $\pm 5 \text{ mm}$ travel was used.

At intermediate strain rates, a custom-built hydraulic press was used. The force was measured using a static load cell located at the top of the press. The piston of the hydraulic system pushes the moving anvil upwards compressing the specimen, which is sandwiched between the moving anvil and the load cell, at a pre-set speed and displacement. The displacement of the moving anvil was measured using calibrated linear variable differential transformers (LVDTs).

Further details of the SHPB and the DIHPB configurations used for high-rate experiments can be found in Refs. [12,31–33] respectively. However, specific details of these experiments are presented here.

The SHPB experiments used Ti–6Al–4V alloy bars with a diameter of 12.7 mm. The striker bar was 400 mm long, the input bar was 1000 mm and the output bar was 500 mm. The striker bar was able to reach speeds up to 20 m s^{-1} , corresponding to an average strain rate of around $4 \times 10^3 \text{ s}^{-1}$. The input and output bars were instrumented with both surface strain gauges (located in the centre of the input bar and 50 mm from the end of the output bar) and piezoelectric gauges, at the specimen-bar interface; Appendix A.4 shows a comparison of data from the bar gauges and piezoelectric gauges. Specimens were sandwiched between the input and output bars with the interfaces lubricated using a thin layer of petroleum jelly, which has previously been shown to be effective at reducing friction [34]. Furthermore, thin copper pulse shapers were used to remove high frequencies from the loading pulse.

With the length of bars described above for the SHPB, it can be challenging to probe large strains, because the duration of the experiment is fixed. To circumvent this issue, DIHPB experiments were performed, in which the striker bar impacts the specimen directly, sending a transmitted signal through to the output bar. Digital Image Correlation (DIC), using images taken with a Photron SA5 high speed camera running at 60,000 frames per second, was used to determine the bar velocities from which the specimen strain was calculated. To enable this, stickers with speckle patterns printed on them were fixed at the ends of each bar. By post-processing these images, time-resolved velocity measurements can be obtained for both bars. These velocities are subsequently used for analysis, alongside the piezoelectric gauge on the output bar, to determine the stress-strain profile.

All stress-strain data in this paper are shown as true stress-true strain.

5.1.2. Varying rate data

The results of the room temperature experiments for the U-NR and the four grades of particulate composites are presented in Figs. 12–14 as true stress vs true strain curves.

From these experiments, the rate dependence in compression for the various grades of rubber can be obtained. As expected, the higher the rate, the greater the strength of the material. The addition of glass microspheres to a 5% volume fraction does not seem to significantly affect the mechanical response. However, further addition to 50% volume fraction suppresses the rubber hyperelasticity. This is since there is less rubber, but also because of the hydrodynamic and interphasial effects in

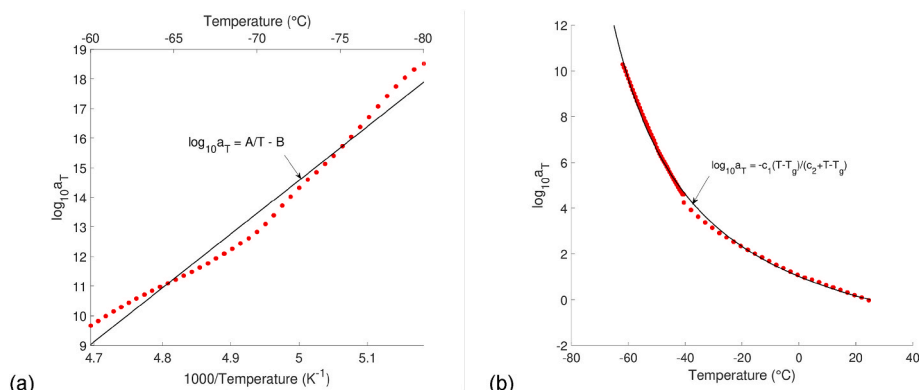


Fig. 9. Shift factors used to construct the master curve for U-NR follow an (a) Arrhenius form below T_g and (b) WLF form above T_g .

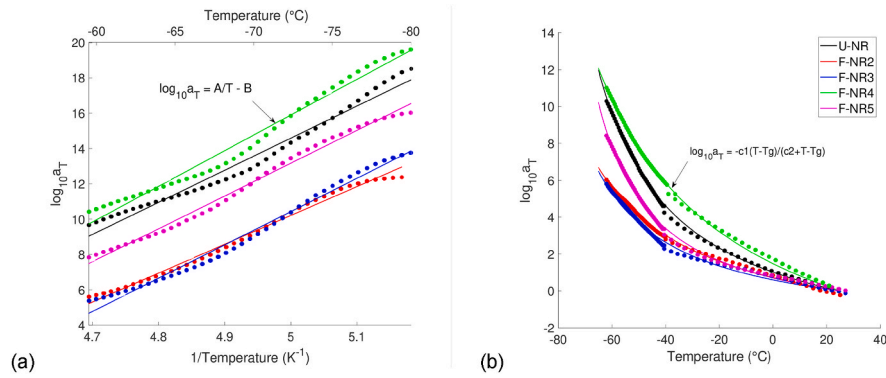


Fig. 10. Comparisons of the shift factors used to construct the master curve for F-NRs (a) below T_g and (b) above T_g .

Table 3

Constants used to fit to the shift factor data presented in Figs. 9 and 10.

Material	Arrhenius constants	WLF constants
U-NR	$A = 18,200 \text{ K}$, $B = 76.3$	$c_1 = 13$, $c_2 = 34 \text{ }^\circ\text{C}$
F-NR2	$A = 16,000 \text{ K}$, $B = 71.5$	$c_1 = 9$, $c_2 = 46 \text{ }^\circ\text{C}$
F-NR3	$A = 18,900 \text{ K}$, $B = 83.9$	$c_1 = 8$, $c_2 = 37 \text{ }^\circ\text{C}$
F-NR4	$A = 20,200 \text{ K}$, $B = 85.1$	$c_1 = 17$, $c_2 = 56 \text{ }^\circ\text{C}$
F-NR5	$A = 18,000 \text{ K}$, $B = 79.8$	$c_1 = 10$, $c_2 = 26 \text{ }^\circ\text{C}$

Table 4

Comparison of the glass transition activation energies resulting from analysing the shifting of the loss tangent peaks, and from the empirical storage modulus shift factor relationship below T_g (fitting constants in Table 3).

Material	Fitting constants	Loss tangent (kJ mol ⁻¹)	Shift factors (kJ mol ⁻¹)
U-NR	$C = 25,000 \text{ K}$, $D = 110$	208	151
F-NR2	$C = 27,000 \text{ K}$, $D = 120$	224	133
F-NR3	$C = 25,000 \text{ K}$, $D = 120$	208	157
F-NR4	$C = 25,000 \text{ K}$, $D = 120$	208	168
F-NR5	$C = 26,500 \text{ K}$, $D = 120$	220	150
Mean	N/A	214	152

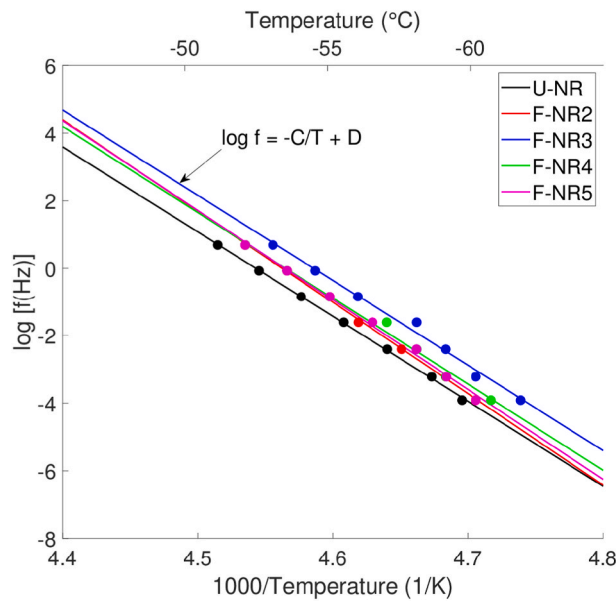


Fig. 11. Using the loss tangent peaks to find the activation energy for the glass transition in U-NR and the four F-NRs.

which the presence of the filler creates a local concentration of the polymer network surrounding the filler that is stiffer than the bulk elastomer [35].

To enable simpler comparison of the materials, selected data showing the rate-dependent response for all grades of NR is shown in Fig. 15. At 10^{-3} s^{-1} , the 5% filled composites both show a slight decrease in yield stress compared to the U-NR. This could be due to a small amount of filler causing degradation in the bulk polymer network, however the difference is small and likely due to experimental variation. At c. 2000 s^{-1} , the mechanical response for the 5% F-NRs is very similar to that of the U-NR.

The apparent modulus can be calculated from the experimental data, taking into account results up to 10% true strain. The modulus is

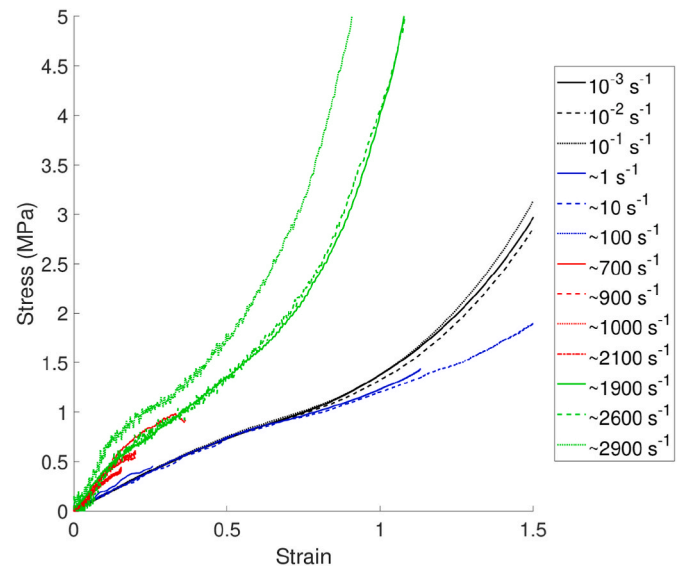


Fig. 12. Varying strain rate data at $25 \text{ }^\circ\text{C}$ for U-NR.

apparently 20% larger than the U-NR. For the 50% F-NRs, at 10^{-3} s^{-1} , the apparent modulus is 5 times larger in the F-NR4/5 compared to the F-NR2/3 and U-NR. At c. 2000 s^{-1} , the apparent modulus is 9 times larger. It should, however, be noted that moduli calculated from compression experiments on short samples are prone to be inaccurate, and are useful mainly for comparison between the four different materials.

A further observation relates to the difference in response for the

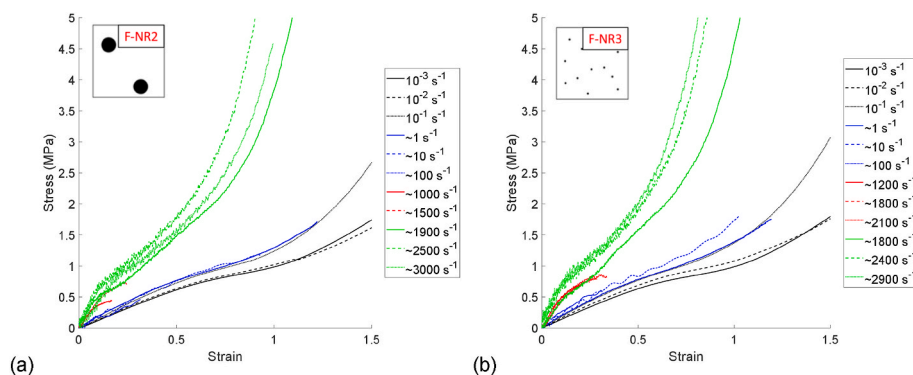


Fig. 13. Varying strain rate data at 25 °C for the 5% filled composites: (a) F-NR2 and (b) F-NR3.

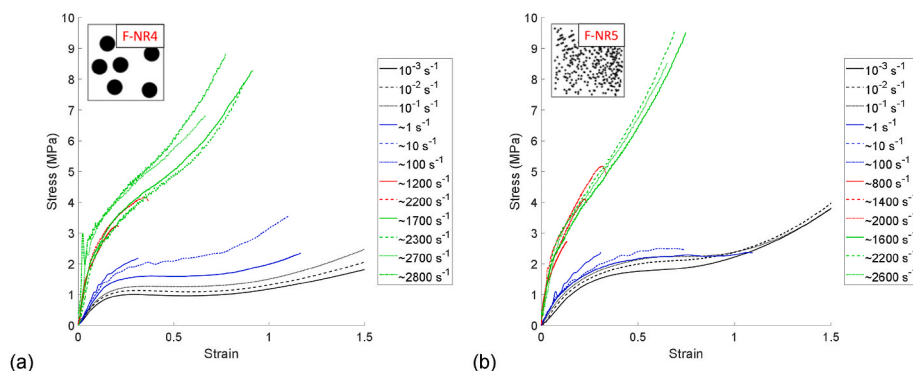


Fig. 14. Varying strain rate data at 25 °C for the 50% filled composites: (a) F-NR4 and (b) F-NR5.

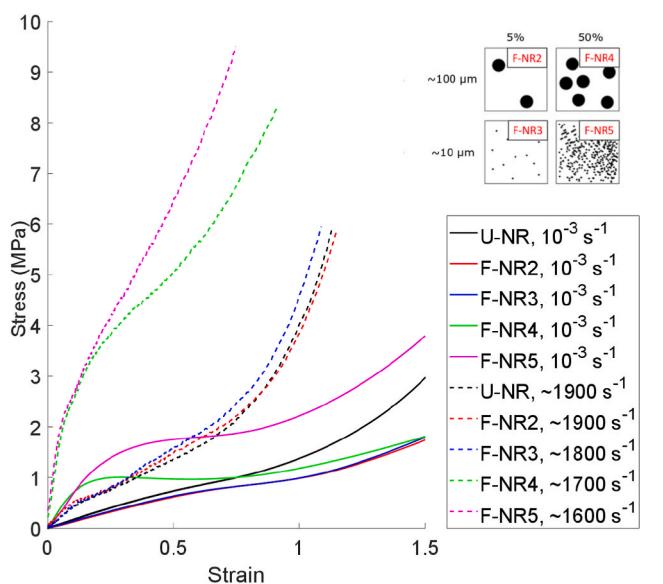


Fig. 15. Highlighting selected varying strain rate data for all grades of NR.

50% F-NRs with differing particle size distributions. At 10^{-3} s^{-1} and c. 2000 s^{-1} , the response for both grades of F-NR is the same up to 10% true strain. However, beyond this, the performance of the F-NR5 exceeds that of the F-NR4. A consequence of this strain induced damage is that F-NR4 is only stronger than the unfilled rubber up to a strain of 75%. After this point, the performance is actually worse for the reinforced rubber than that of the unfilled rubber.

5.2. Temperature dependence

5.2.1. Experimental techniques

At low strain rates, varying temperature experiments were conducted using an Instron 3119-600 Series environmental chamber. This chamber features a Eurotherm 3208 temperature controller with closed loop control provided by a Type N thermocouple inside the chamber to monitor the temperature. As this thermocouple was situated in air at the rear of the chamber, its reading was prone to system hysteresis with fluctuations of $\pm 3.5^\circ\text{C}$; a second thermocouple was integrated into the loading platen to give $\pm 1^\circ\text{C}$ confidence.

For experiments at sub-ambient temperatures, the chamber was connected to a liquid nitrogen dewar. The cold nitrogen gas was fed into the chamber where it cooled the interior by convection. For supra-ambient temperatures, the chamber's in-built forced convection heater was used.

Each sample was held at temperature for a minimum of 30 min to ensure thermal stability. Experiments were only started once the two thermocouple readings were within 0.5°C of each other, ensuring that the temperature is stable inside the chamber.

To interrogate further the relationship between rate and temperature, an ancillary cooling device for the SHPB, comprising a liquid nitrogen immersion chiller and a bespoke fixture was created to conduct low temperature, high rate experiments (Fig. 16). Using the device, oxygen-free nitrogen gas was fed through silicone hosing into a copper coil submerged in liquid nitrogen, all contained within a thermally insulating Nalgene® dewar. The cooled nitrogen gas was then directed through an opening on the top of the fixture, where it subsequently cooled the specimen down to a minimum of -100°C .

5.2.2. Data from lower rate experiments

Low temperature experiments at a low strain rate of 10^{-2} s^{-1} were performed over a temperature range from -80°C to -40°C in order to



Fig. 16. Bespoke fixture for the SHPB to contain the sample for low temperature, high rate experiments.

cover the transition region. Three runs were carried out at each temperature.

In comparing the results of the U-NR (Fig. 17) to the results of the 5% filled F-NRs (Fig. 18), it is evident that the mechanical response is qualitatively the same. The dominant influence on the behaviour is the glass transition of the rubber. When the temperature is below -50°C , the strength and modulus are significantly higher than above this

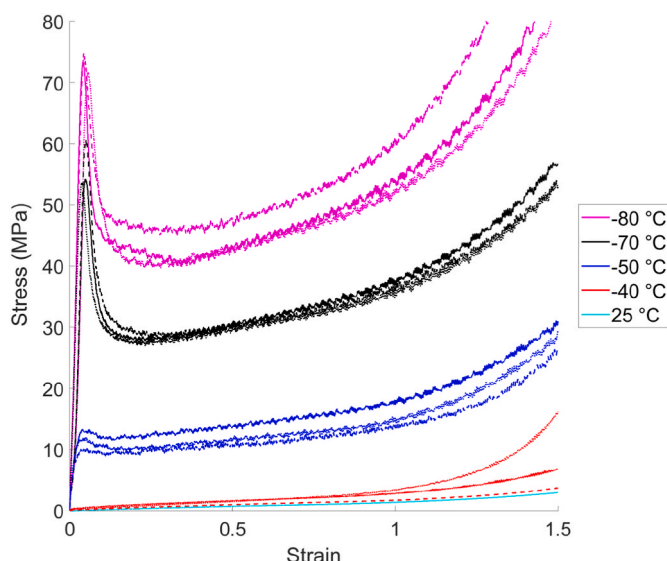


Fig. 17. Low rate, varying temperature results for U-NR.

temperature. In fact, in Fig. 17, the results at -50°C show the onset of the glass transition's influence.

Qualitatively, the lower the temperature, the higher the peak stress. There does appear to be a slight decrease in strength for the F-NR3 (Fig. 18b) compared to the F-NR2 (Fig. 18a) suggesting there may be an influence of the mean particle size, however this needs to be more carefully studied: the scatter in the data obtained from experiments below -50°C make comparisons of the peak stress between the grades of rubber difficult. Comparisons are shown in §5.1.3. There are two expected reasons for this scatter: firstly, the addition of fillers with a given particle size distribution leads to stress variations across the cross-section and between samples; and secondly, the influence of the glass transition makes the response very sensitive to small changes in the temperature. This is particularly observed in the results at -60°C in Fig. 18; DMA (§3.2) and DSC (§3.1) data have shown that this is within the transition region for this natural rubber.

The results for the 50% filled particulate composites can be seen in Fig. 19. Similar observations can be made as with the less filled composites. Most interestingly, for the composite with smaller particles (F-NR5, Fig. 19b), intermediate behaviour can be seen in the response at $T \approx -55^{\circ}\text{C}$. This is believed to be due to an insufficient hold time between closing the environmental chamber door after placing this specimen, and starting the experiment. This has led to a unique condition where the temperature is slightly higher at the start compared to the end. This provides more evidence for the high temperature sensitivity around the T_g for the rubber.

In order to better compare the low temperature quasi-static experiments for all grades of rubber, selected data at -80°C , -40°C and 25°C are plotted in Fig. 20. At -40°C , filler fraction has more of an influence on the response than does the mean particle size (i.e. NR4 and NR5 are observed to be very similar to each other, as are NR and NR3). This is also seen in Fig. 21. The 5% filled composites show a smaller increase in modulus compared to the 50% filled composites.

At -80°C , the mean particle size appears to affect the peak stress: the samples with larger particles retain the strength seen with the U-NR. Those with smaller particles have a lower peak stress, although, as explained before, these findings need further scrutiny owing to scatter. The filler fraction influences the post-yield response, with the 5% filled composites both showing a sharp drop after the peak stress and a steep strain-hardening response, similar to that of U-NR. The 50% filled composites show a gradual reduction in stress over a larger range of strain followed by a similar strain-hardening gradient. At the largest strains, it appears as though the materials with smaller particles have a steeper strain-hardening gradient than that of those with larger particles. The softening is likely to be a result of post-yield softening in the polymer, which is now below its glass transition temperature, combined with debonding of the particles. The hardening is usually ascribed to chain alignment in the polymer.

5.3. Data from higher rate experiments

Results of high strain rate experiments conducted at -40°C for all grades of rubber are shown in Fig. 21. The difference between a strain rate of $c. 1000\text{ s}^{-1}$ and $c. 2000\text{ s}^{-1}$ does not seem to affect the apparent stiffness. This is because the rubbers are already in their glassy state and so the influence of a further increase in rate is small. This is consistent with the results of DMA experiments shown in §3.2.

Filler volume fraction has more of an effect on the apparent stiffness. Calculating the initial moduli for all grades of rubber (at 1% true strain), it is observed that the values for the 5% F-NRs are on average 20% higher and those for the 50% F-NRs are 3 times higher than that for the U-NR. At -40°C , the stiffness enhancement due to filler volume fraction is not as significant as the change at 25°C . This is because the decrease in temperature has already contributed to stiffness enhancement, and as the rubber becomes glassy, there is a limit to how much the stiffness can be enhanced. This limiting glassy stiffness can be seen in the results of

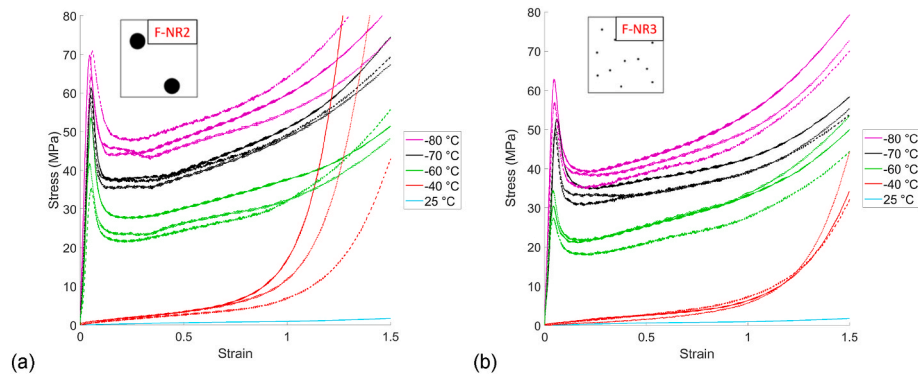


Fig. 18. Low rate, varying temperature results for the 5% filled composites: (a) F-NR2 and (b) F-NR3.

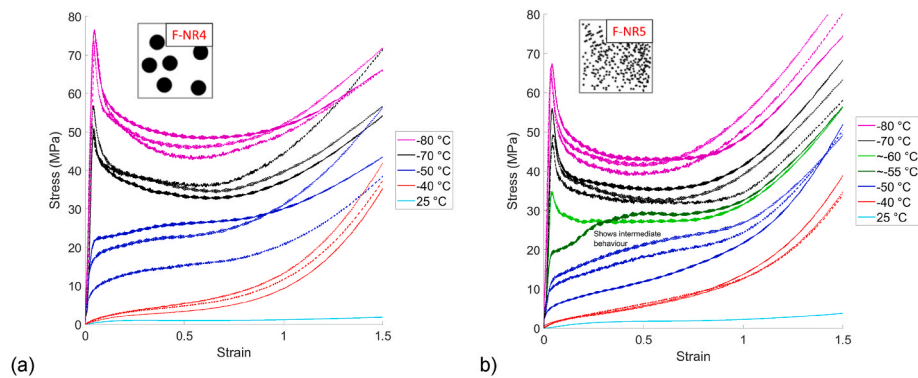


Fig. 19. Low rate, varying temperature results for the 50% filled composites: (a) F-NR4 and (b) F-NR5.

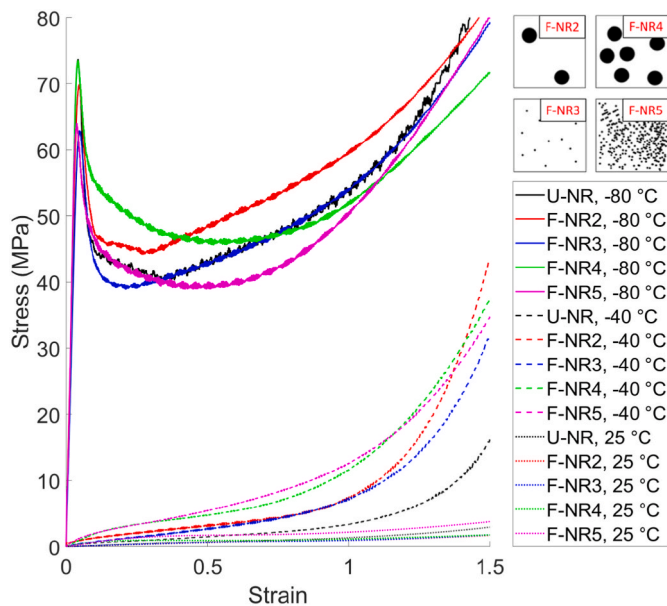


Fig. 20. Highlighting selected low rate, varying temperature data for all NR grades.

the varying temperature experiments (Fig. 20) and also in the DMA results, with the low temperature plateau.

For use in damage analysis later in this paper (§5.1.2), selected data for high strain rate experiments conducted using the SHPB at $-60\text{ }^{\circ}\text{C}$ are shown in Fig. 22.

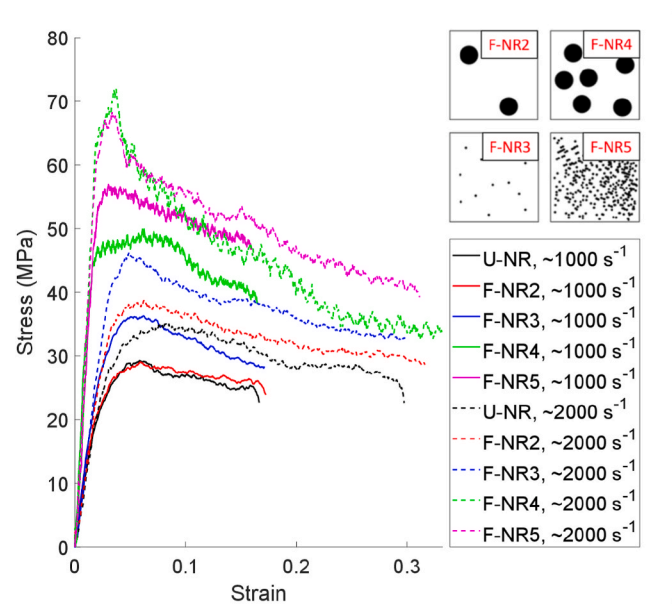


Fig. 21. Comparison of high strain rate data from SHPB experiments at $-40\text{ }^{\circ}\text{C}$ for all grades of NR.

5.4. Interrupted experiments

Literature suggests that the main form of damage in these particulate composites is strain activated debonding of the particles from the matrix [36,37]. In order to experimentally characterise this damage, and compare across strain rates, interrupted experiments were performed to a number of different final strains at a strain rate of 10^{-2} s^{-1} and $25\text{ }^{\circ}\text{C}$.

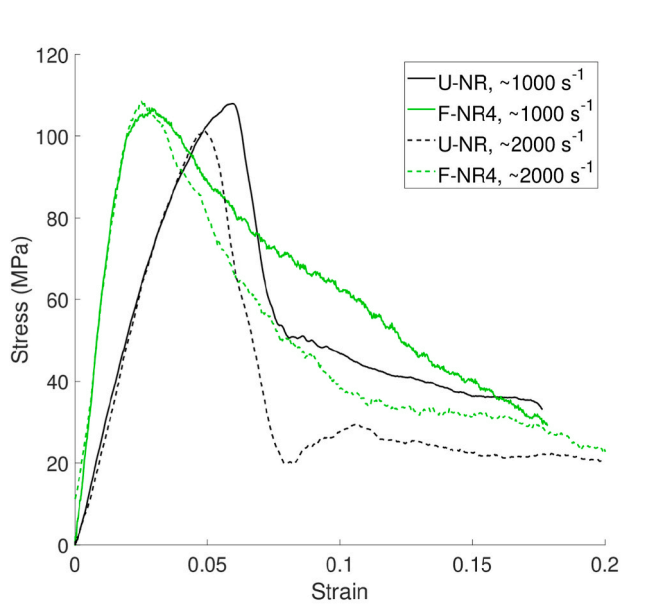


Fig. 22. Comparison of high strain rate data from SHPB experiments at -60°C for the unfilled (U-NR) and 50% large particle filled (F-NR4) materials.

Nine experiments were conducted for each grade of rubber, three for each value of maximum nominal strain: $e = 0.1, 0.2, 0.3$. Selected retrieved samples were then subsequently scanned using X-ray micro-Computerised Tomography to better visualise the extent of damage (§4.4.1). Results of these interrupted experiments can be found in Appendix A.5.

Experiments at high strain rates up to a final nominal strain of 0.3 have also been conducted using the SHPB. The purpose of these is to compare the extent of strain activated damage at high rates and low temperatures to interrogate the rate-temperature equivalence of damage further. The recovered specimens from these SHPB experiments were also used for post-test assessments. This process is detailed below.

5.5. Post-test damage assessment

In order to interrogate the extent of damage at nominal strains of 0.3, experiments using X-ray micro-Computerised Tomography (μCT) were performed to visualise the internal damage and calculate the volume fraction of various phases. Additional quasi-static experiments at room temperature were also conducted on recovered specimens from both sets of experiments (sub-ambient/quasi-static and ambient/SHPB) to measure their residual strength and better understand the extent of damage.

5.5.1. X-ray micro-Computerised Tomography (μCT)

A ZEISS Xradia 510 Versa 3D X-ray microscope was used to obtain tomographs for four conditions: quasi-static, ambient temperature; quasi-static, low temperature; high rate, ambient; and untested. The Versa can reach spatial resolution of $0.7\text{ }\mu\text{m}$ and is equipped with a 5 kN Deben load stage. This was used to apply a small load (c. 7 N) during the scan to deform the samples by 0.5 mm enabling the voids to open facilitating imaging. Scans averaged 15 h with 1x binning (50 kV, 4.5 W power, 30 – 34 s per radiograph, no filter except for the glassy carbon of the Deben tube, 1601 radiographs recorded over 360° , resulting in a $5.3\text{ }\mu\text{m}$ voxel size and a reconstructed volume of $5.4 \times 5.4 \times 5.4\text{ mm}^3$). For this reason, F-NR4 was chosen as it was the 50% filled composites with larger particles enabling better resolution imaging.

A magnified visualisation of a single 2D slice from the scanned F-NR4 sample initially tested to a nominal strain of 0.3 at high rates using the SHPB is shown in Fig. 23. It has been annotated to highlight the rubber matrix, glass filler and void phases.

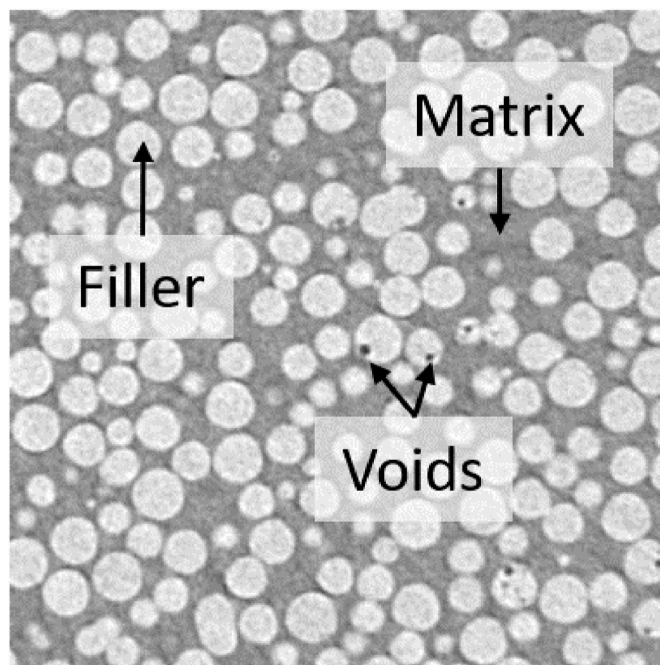


Fig. 23. A magnified view of a single 2D slice from the μCT scanned F-NR4, which was compressed using a SHPB, showing the matrix, fillers and voids.

A 3D visualisation was produced for this scanned sample using the Thermo Scientific Avizo 2020.3.1 software and is shown in Fig. 24a. Once rendered in 3D, an unsupervised k-means clustering algorithm was used to classify the composite into three phases: rubber, glass microspheres, and voids. This segmentation is shown in Fig. 24b. Upon segmenting the composite into its constituent phases, the volume fraction for each phase can be calculated. The same process is used for the three other conditions considered in this study and their volume fractions are presented in Table 5.

Upon analysing the volume fractions, it appears as if there is a significant void fraction for even the untested sample. Although, the void fraction increases for the three samples that were compressed, only the quasi-static, low temperature sample showed a significant increase, implying it experienced the greatest damage. Whereas, the void fraction for the quasi-static and the high rate ambient samples are essentially the same, implying a similar extent of damage. To interrogate this further, the next section details the results of residual strength experiments.

5.5.2. Residual strength experiments

The untested F-NR4 and recovered samples from the same conditions as above were also subjected to residual strength experiments. Here, the samples were compressed to a nominal strain of 0.5 at 25°C and a strain rate of 0.01 s^{-1} . By comparing the response of each to that of a previously untested sample, the extent of damage suffered by the sample under each condition can be better understood. Fig. 25 shows the results of these residual strength experiments.

From these experiments, it appears that the extent of damage for both samples previously tested at 25°C is similar regardless of the strain rate. This finding is consistent with the similar void volume fractions found in the μCT study. However, the effect of damage for a sample compressed at -45°C is less than both the others, which is not what was observed in the μCT study where the void fraction for this sample was 5% points higher.

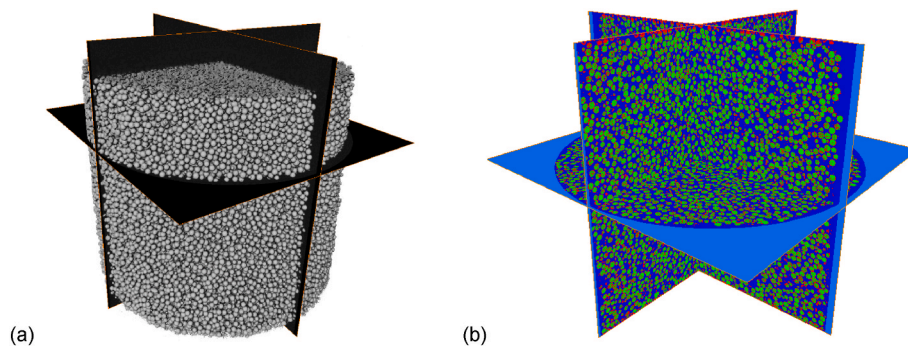


Fig. 24. (a) 3D visualisation of μ CT scanned F-NR4, which was compressed using a SHPB and (b) the result of the classification algorithm, where: dark blue is rubber; green represents the glass microspheres; and in pink are the voids. (For interpretation of the references to colour in this figure legend, the reader is referred to the Web version of this article.)

Table 5

Volume fractions calculated for the four different F-NR4 samples: quasi-static, ambient; quasi-static, low temperature; high rate, ambient; and untested.

Material	Volume Fraction (%)		
	Rubber	Glass	Voids
Untested	50.5	34.2	15.3
Quasi-static, ambient	52.0	31.5	16.5
Quasi-static, low temperature	52.2	25.7	22.1
High rate, ambient	50.5	33.2	16.3

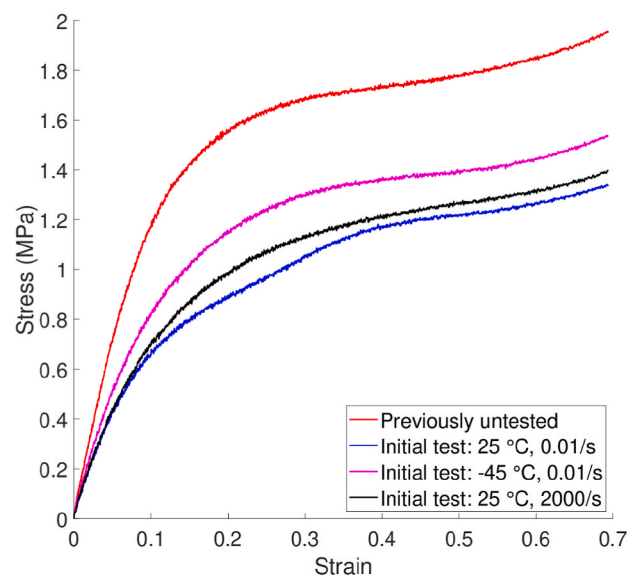


Fig. 25. Comparing the residual strength responses of F-NR4 at 25 °C for samples which were previously compressed under various conditions.

6. Discussion

6.1. Rate-temperature equivalence

As was briefly described in the Introduction, and shown experimentally in §3.2, a rate-temperature equivalence exists in these materials. This equivalence allows the construction of a TTS based master curve showing the modulus as a function of frequency. In this section, the rate-temperature equivalence will be further explored in terms of the stress-strain profiles, damage evolution and yield stress.

6.1.1. Stress-strain behaviour

The rate-temperature equivalence in the materials is explored by comparing quasi-static stress-strain data obtained at reduced temperature to the data from room-temperature SHPB experiments. An overall, large strain comparison of low temperature quasi-static and room temperature SHPB data is provided in Fig. 26.

For U-NR and F-NR3, the mechanical responses of quasi-static compression experiments conducted at -40 °C correlate well with the high strain rate experiments performed on the SHPB at 25 °C. However, for F-NR2, the temperature appears to be slightly too low to accurately match the high rate data. There is some noise in the high rate data and variation in the low temperature experiments that make it difficult to identify the exact value of temperature required to simulate perfectly the high rate response.

For the 50% F-NRs, the rate-temperature equivalence is excellent. Here, quasi-static experiments were performed at -45 °C to take into account the enhancement with a higher filler volume fraction. This equivalent temperature was obtained using insights from the DMA experiments along with iterative experimentation.

Except for the F-NR2 (likely due to the slightly lower temperature as explained before), there is excellent agreement for all grades of materials. This implies that not only is there a rate-temperature equivalence for the modulus, but the same equivalence exists for the damage and

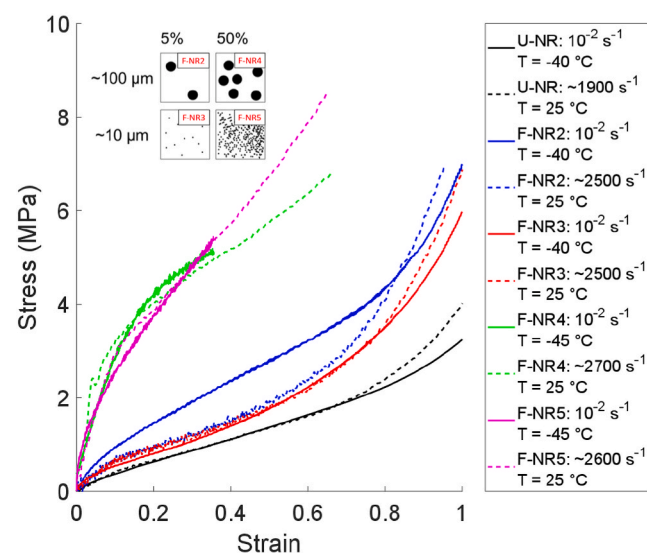


Fig. 26. Showing that experimentally simulating the high rate response of all grades of NR is possible with the use of low temperature quasi-static analogue experiments.

strain hardening mechanisms. This observation is key to enable a TTS based modelling framework to be developed in order to predict the stress-strain response for particulate composites at high strain rates.

6.1.2. Damage analysis

At $-40\text{ }^{\circ}\text{C}$ and high strain rates, it was observed (Fig. 21) that the post-yield strength reduction is essentially the same for all materials (taking into account any experimental variations). This is as the slopes of the stress-strain curves beyond yield are qualitatively parallel to each other.

At $-60\text{ }^{\circ}\text{C}$, the focus is F-NR4 as it was the material that the μCT study was conducted on. Its behaviour is compared to the results of the unfilled material (Fig. 22). The elastic behaviour is similar at both rates, but the post-yield behaviour is affected by the increase to $c. 2000\text{ s}^{-1}$ in that the extent of damage is larger.

The lower strengths of F-NRs with larger mean particle size in Fig. 21 is expected to be due to strain induced debonding. Since the surface to volume ratio is ten times higher for F-NR3/5 compared to F-NR2/4, their interfacial bond strengths are greater. Hence, strain induced debonding is hypothesised to cause the decreased performance for F-NRs with larger particles. It is debonding, rather than filler fracture, that is expected to be the dominant failure mechanism. Previous literature [36] has shown that deformations in the filler are minimal when fillers are significantly stiffer than the binder as in this case (69 GPa vs 0.52 MPa), and that the fillers realign by rotating and sliding to accommodate the larger deformations in the matrix. This leads to debonding between the rubber and the filler material.

Post-mortem examinations can be conducted for each experiment to visualise simply the extent of damage. At $-40\text{ }^{\circ}\text{C}$, there was no observable damage even though experiments were performed at high strain rates using the SHPB. However, at $-60\text{ }^{\circ}\text{C}$, extensive damage was evident. Photographs for U-NR are shown in Fig. 27, with those for the other materials provided in Appendix A.6.

For the U-NR, catastrophic damage is only seen at the higher strain rate (Fig. 27b). This is also evident from the stress-strain data in Fig. 22, which shows a sharp drop in strength for the sample compressed at $c. 2000\text{ s}^{-1}$. For F-NR2, samples at both strain rates showed similar damage. At $c. 1000\text{ s}^{-1}$, though there was a fracture running across the sample, it was held together by some of the rubber, whereas at $c. 2000\text{ s}^{-1}$, the rubber was unable to hold the pieces of the sample together. For F-NR3, the sample compressed at $c. 1000\text{ s}^{-1}$ did not show any damage at all. However at $c. 2000\text{ s}^{-1}$, catastrophic failure occurred and the sample split into two pieces, showing a similar diagonal fracture to other failures. For F-NR4, both samples showed extensive damage. At $c. 1000\text{ s}^{-1}$, a diagonal fracture split the sample into two pieces held together by a small amount of rubber spanning the fracture plane. At $c. 2000\text{ s}^{-1}$, catastrophic failure was observed where the sample has been completely destroyed into many small pieces, albeit still held together by the rubber

matrix. F-NR5 showed a similar type of failure as the other samples that failed. A diagonal fracture plane was observed at approximately 45° to the axis of compression.

The presence of diagonally oriented fracture planes points to failure induced by adiabatic shear instability. Due to the low thermal diffusivity of natural rubber ($k \approx 10^{-7}\text{ m}^2\text{ s}^{-1}$ [25]), adiabatic conditions are present at relatively low strain rates. Given a sample with a 2.5 mm length-scale (half of the diameter/length), adiabatic conditions would exist at strain rates over $c. 10^{-2}\text{ s}^{-1}$. This means that in high strain rate experiments, the sample heats up due to internal plastic dissipation and the inability for the heat to diffuse out of the sample during the time-scale of the experiment, which may subsequently lead to thermal softening and unstable growth of localised shear bands [38].

To estimate the temperature rise, the mechanical work done on the U-NR sample for a compression experiment at $c. 2000\text{ s}^{-1}$ is calculated (to a stress of 100 MPa and strain of 0.05), and divided by the density (966 kg m^{-3}) and heat capacity (shown in §3.1 to be $925\text{ J kg}^{-1}\text{ }^{\circ}\text{C}^{-1}$ at $-60\text{ }^{\circ}\text{C}$), to give a temperature rise just under $3\text{ }^{\circ}\text{C}$. Though this seems small, it has been shown earlier with the results of varying temperature compression experiments (e.g. Fig. 19b), that small changes in temperature around the T_g significantly affect the mechanical response. Furthermore, it was shown in §3.2 that the modulus for U-NR can drop by as much as 60% by increasing the temperature by $3\text{ }^{\circ}\text{C}$ from $-60\text{ }^{\circ}\text{C}$.

The perturbation analysis of Bai [39] found that adiabatic shear instability occurs when the thermal softening rate exceeds the strain hardening rate. Since thermal softening rapidly occurs through the T_g , by starting the high rate compression experiments just below the T_g of U-NR, it is possible to induce this instability and observe the shear based failures as shown above.

This shear localisation instability can also occur at lower temperatures due to a negative strain hardening rate from microcrack and craze formation [40] due to the particulate nature of the material. In future, further experiments at temperatures below T_g could be conducted allowing a more thorough post-mortem examination of the fracture surface to determine whether localised melting or brittle fracture is observed.

6.2. Variation of peak stress

It is common in literature to quote the values of peak stress, yield stress or a characteristic stress against the temperature or logarithm of the strain rate [10,41,42]. For this reason, to facilitate comparisons and discussion, Figs. 28–30 show the peak stresses against these two variables for all grades of NR. Appendix A.7 shows Eyring plots giving the same data as a function of strain rate for the room temperature experiments. Where the data did not show the sample yielding, a characteristic stress (value at $\epsilon = 0.1$) is shown instead. As expected, peak stress increases with increasing strain rate and decreasing temperature.

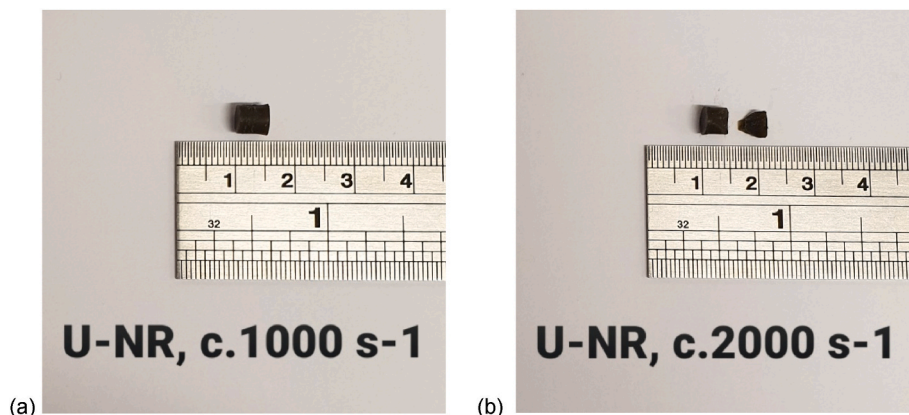


Fig. 27. Post-mortem examination for high strain rate experiments at $-60\text{ }^{\circ}\text{C}$ for U-NR at (a) $c. 1000\text{ s}^{-1}$ and (b) $c. 2000\text{ s}^{-1}$.

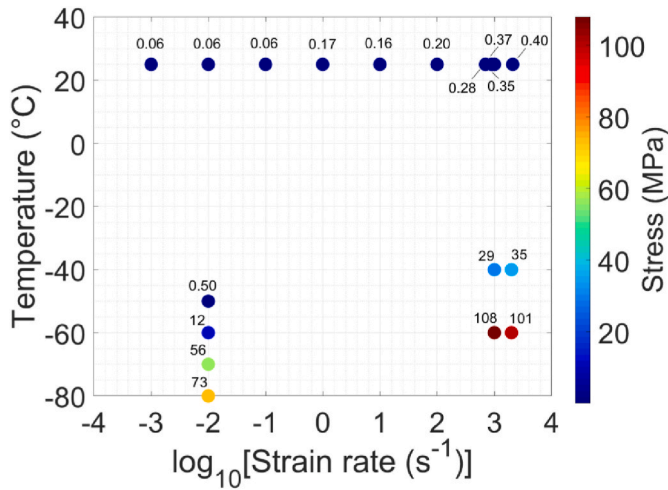


Fig. 28. Strain rate and temperature dependence on the peak stress for U-NR.

Note that, as explained in §4, the experimental variation with temperature below $-50\text{ }^{\circ}\text{C}$ makes comparisons of the peak stress between the various grades of rubber difficult. Therefore, the purpose of plotting the temperature dependence of the peak stress is to show the relative changes, rather than the absolute values.

6.3. Enhancement of the apparent modulus

The general behaviour of filler modulus enhancement has been extensively studied in past research [43–46], albeit with a focus on linearly elastic fillers and binders.

The modulus enhancement observed in the varying strain rate experiments can be compared to the result of the Guth modified Einstein-Smallwood relation as shown in Equation (3):

$$E = E_m \left(1 + 2.5\phi_f + 14.1\phi_f^2 \right) \quad (3)$$

where E_m is the modulus of the natural rubber matrix and ϕ_f is the filler volume fraction [47,48]. Where the Einstein-Smallwood relation predicted the modulus of particle filled solids at low volume fractions, the Guth modification extends its application to higher volume fractions. Einstein initially derived the increase in viscosity caused by rigid spherical particles in a viscous liquid. Further modifications to the relation followed in order to incorporate interactions with neighbouring particles.

At 10^{-3} s^{-1} and 5% volume fraction, this relation gives the modulus enhancement to be 16%. Whereas at 50% volume fraction, the enhancement is 5.8 times the matrix modulus ($5.8 E_m$). The apparent modulus enhancement observed experimentally (Fig. 15) at both low and high rates for the 5% F-NRs is insignificant. The enhancement for the 50% composites at a low rate is c. $5 E_m$ and similar to that predicted by the Guth relation. However, at the larger strain rate, the apparent modulus enhancement observed ($9.1 E_m$) exceeds the prediction from the Guth relation. This may be analogous to the particle aggregation phenomenon described by Guth: the clustering of particles leading to an even greater stiffness enhancement than expected with perfectly distributed spheres. At high strain rates, the immobility of the polymer network may be giving rise to pseudo-clusters leading to this further enhancement. The Guth model for rod-like shapes (Equation (4)) can be used to characterise these clusters formed by the spheres:

$$E = E_m \left[1 + 0.67f\phi_f + 1.62(f\phi_f)^2 \right] \quad (4)$$

where f is known as the shape factor. Bergstrom estimates the shape factor (=length/breadth) to vary between 4 and 10 [49]. When 4 is used as the factor, the modulus enhancement using Equation (4) yields a 20% rise for the 5% F-NRs and a 9 times increase for the 50% F-NRs. These predictions better match the experimental observations.

Due to the rate-temperature equivalence, modulus is dependent on both the rate and the temperature. For this reason, the above analysis becomes less feasible for experiments conducted at lower temperatures without making appropriate modifications. For example, for low strain rate experiments as shown in Fig. 20, at $-80\text{ }^{\circ}\text{C}$, there appears to be no filler influenced modulus enhancement. However, at $-40\text{ }^{\circ}\text{C}$, the

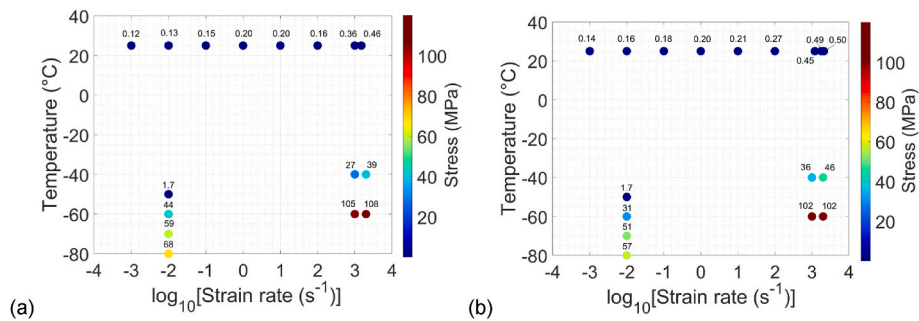


Fig. 29. Strain rate and temperature dependence on the peak stress for the 5% filled composites: (a) F-NR2 and (b) F-NR3.

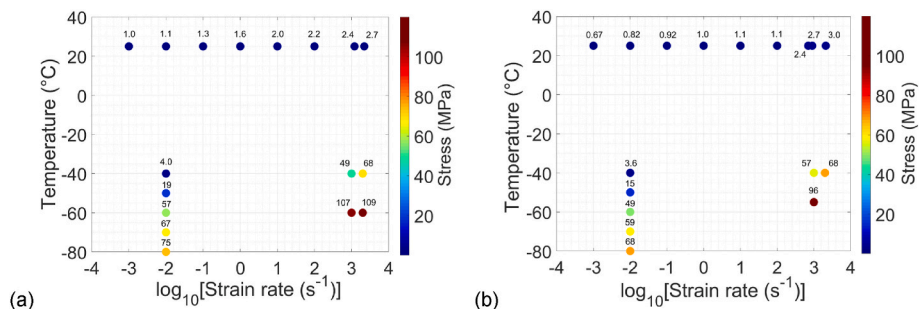


Fig. 30. Strain rate and temperature dependence on the peak stress for the 50% filled composites: (a) F-NR4 and (b) F-NR5.

Table 6Observed apparent modulus enhancements (E/E_m) for various conditions and the required shape factors (f).

	5% F-NRs		50% F-NRs	
	Ambient	−40 °C	Ambient	−40 °C
Low strain rate	$E/E_m = 1.0, f = 1$	$E/E_m = 2.0, f = 12$	$E/E_m = 5.0, f = 3$	$E/E_m = 5.0, f = 3$
High strain rate	$E/E_m = 1.0, f = 1$	$E/E_m = 1.2, f = 4$	$E/E_m = 9.1, f = 4$	$E/E_m = 3.0, f = 2$

apparent modulus is on average 2 times larger for F-NR2/3 and 5 times larger for F-NR4/5. If using Equation (4), this corresponds to a shape factor of 12 and 3 respectively. When high strain rate experiments are conducted at the same temperature, the apparent modulus is only 20% larger for the 5% F-NRs and 3 times larger for the 50% F-NRs, corresponding to shape factors of 4 and 2 respectively. Table 6 highlights the observed apparent modulus enhancements for various conditions and the required shape factors.

This means that the sensitivity of the modulus enhancement mechanism drops as temperature is reduced and as strain rate is increased. Furthermore, if using the Guth model for rod-like shapes, this would imply pseudo-clusters that depend on temperature as well as rate. In future, X-ray diffraction and/or scattering techniques can be conducted in-situ during varying rate and varying temperature experiments to validate the existence of these proposed structures.

7. Conclusions

In this paper, the results for the experimental characterisation of unfilled and glass microsphere filled natural rubber materials over a range of strain rates and temperatures are presented.

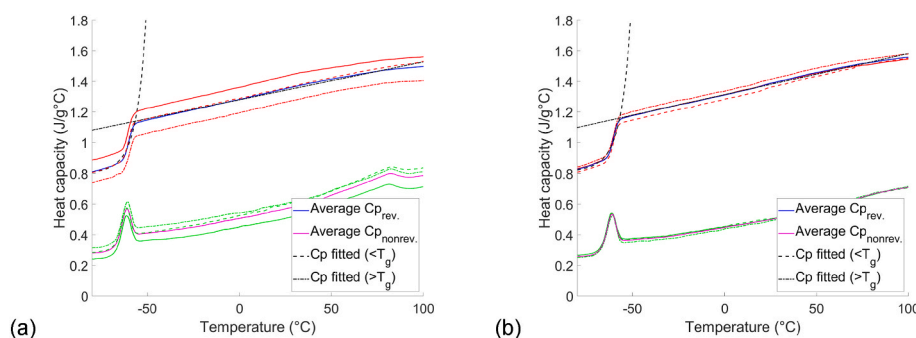
The rate-temperature equivalence based on uniaxial, compressive and DMA experiments was explored. Due to this equivalence present in the stress-strain response, it is likely that the rate-temperature dependence for the damage and strain hardening mechanisms are the same as that for the modulus. Therefore, the DMA based shift factors for the modulus may be used to develop a predictive model for these materials.

Furthermore, the effect of filler volume fraction and mean particle diameter on the rate and temperature dependence of the overall mechanical response was also investigated. The enhancement of the apparent modulus due to the addition of fillers was observed, and a theory discussed, which could allow this phenomenological effect to be incorporated into future modelling strategies.

To facilitate models aiming to take into account the effect of temperature rise due to adiabatic conditions at high strain rates, the results of MDSC experiments were presented. These offer an understanding of the temperature dependent heat capacity, and its influence on calculated temperature rises.

Appendices.

A.1. MDSC data

**Fig. 31.** MDSC results for (a) F-NR2, (b) F-NR3 with model fits either side of T_g .

This paper provides experimental insights and data that will inform future constitutive modelling efforts. Furthermore, it is hoped that the experimental results featured in this paper will assist future investigations involving the high rate behaviour of unfilled and filled polymeric materials.

CRediT authorship contribution statement

Akash R. Trivedi: Methodology, Formal analysis, Investigation, Writing – original draft. **Rory Whybrow:** Investigation, Methodology, Writing – review & editing. **Alan H. Muhr:** Resources, Methodology, Writing – review & editing. **Clive R. Siviour:** Conceptualization, Methodology, Resources, Writing – review & editing, Supervision, Project administration, Funding acquisition.

Declaration of competing interest

The authors declare that they have no known competing financial interests or personal relationships that could have appeared to influence the work reported in this paper.

Data availability

Data will be made available on request.

Acknowledgements

This material is based upon work supported by the Air Force Office of Scientific Research, Air Force Material Command, USAF under Award No. FA9550-15-1-0448. Any opinions, findings, and conclusions or recommendations expressed in this publication are those of the author (s) and do not necessarily reflect the views of the Air Force Office of Scientific Research, Air Force Material Command, USAF. The use of facilities funded by EPSRC Grant EP/M02833X/1 “University of Oxford: experimental equipment upgrade” is gratefully acknowledged. The authors are also very grateful to Prof James Marrow from the Department of Materials at the University of Oxford for his advice and helpful discussions.

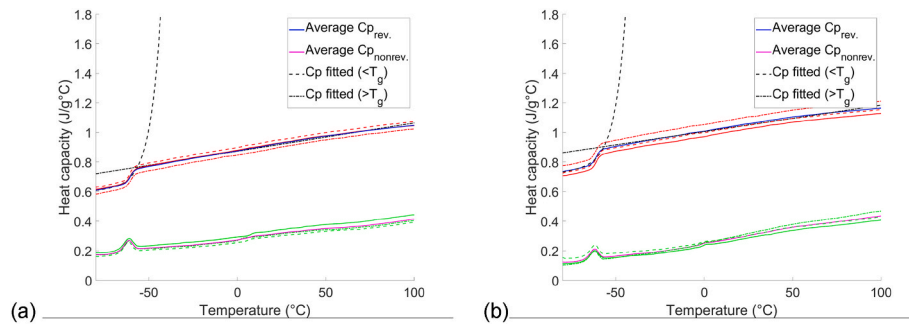


Fig. 32. MDSC results for (a) F-NR4, (b) F-NR5 with model fits either side of T_g .

A.2. DMA storage/loss moduli and loss tangents

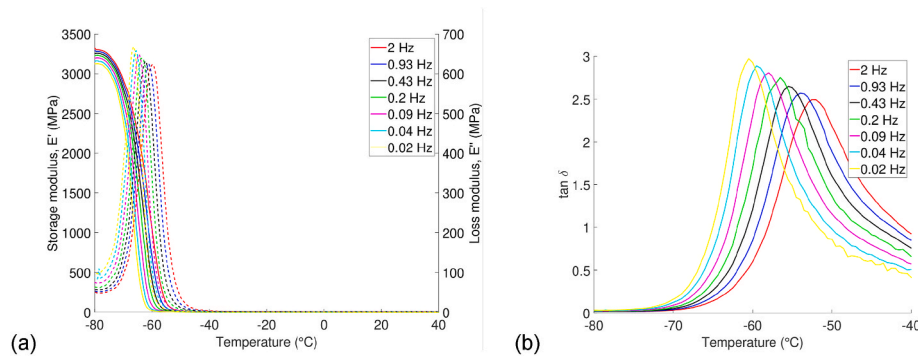


Fig. 33. DMA results for F-NR2: (a) temperature dependent storage (solid line) and loss (dashed line) moduli and (b) loss tangents.

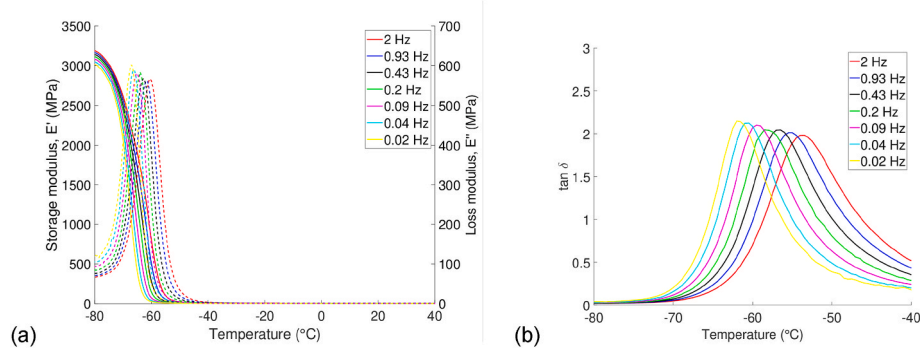


Fig. 34. DMA results for F-NR3: (a) temperature dependent storage (solid line) and loss (dashed line) moduli and (b) loss tangents.

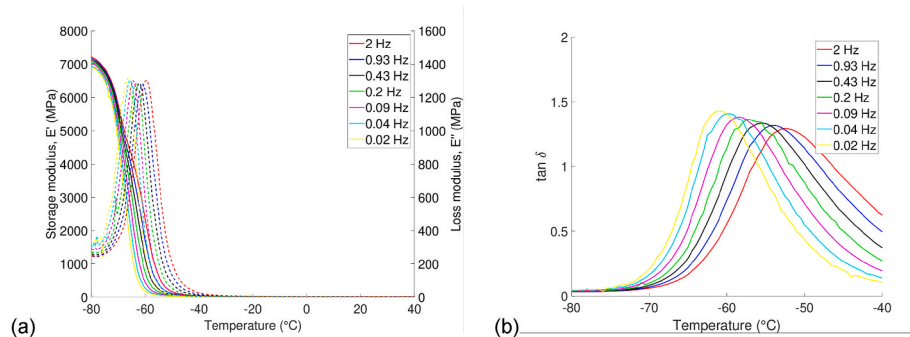


Fig. 35. DMA results for F-NR4: (a) temperature dependent storage (solid line) and loss (dashed line) moduli and (b) loss tangents.

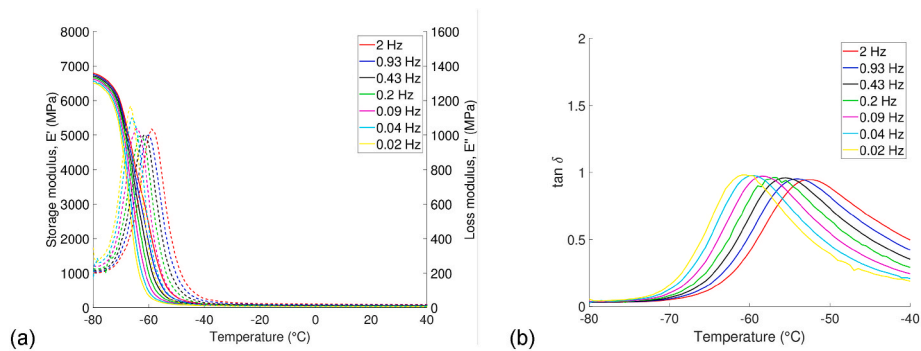


Fig. 36. DMA results for F-NR5: (a) temperature dependent storage (solid line) and loss (dashed line) moduli and (b) loss tangents.

A.3. DMA isotherms

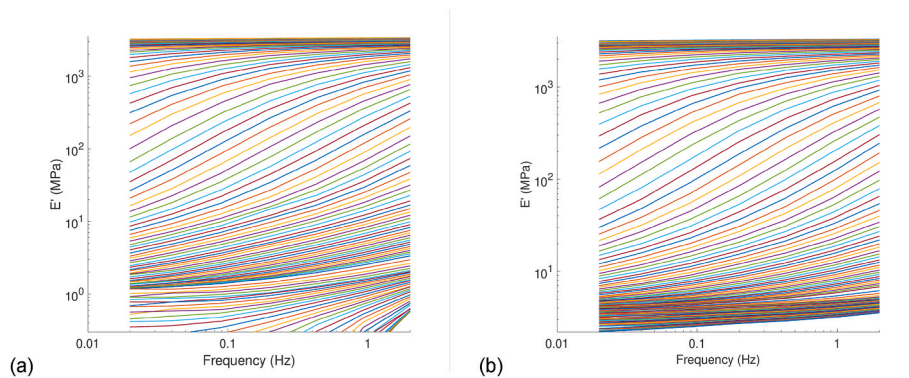


Fig. 37. Isotherms from the DMA results for (a) F-NR2, (b) F-NR3.

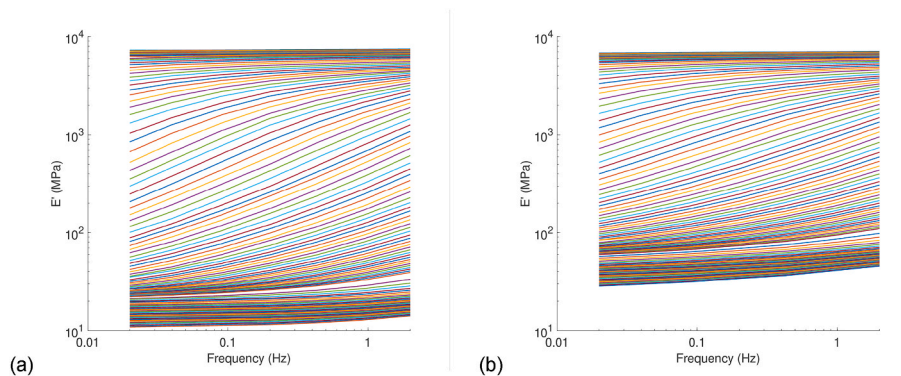


Fig. 38. Isotherms from the DMA results for (a) F-NR4, (b) F-NR5.

A.4. Bar gauge vs Piezoelectric gauge

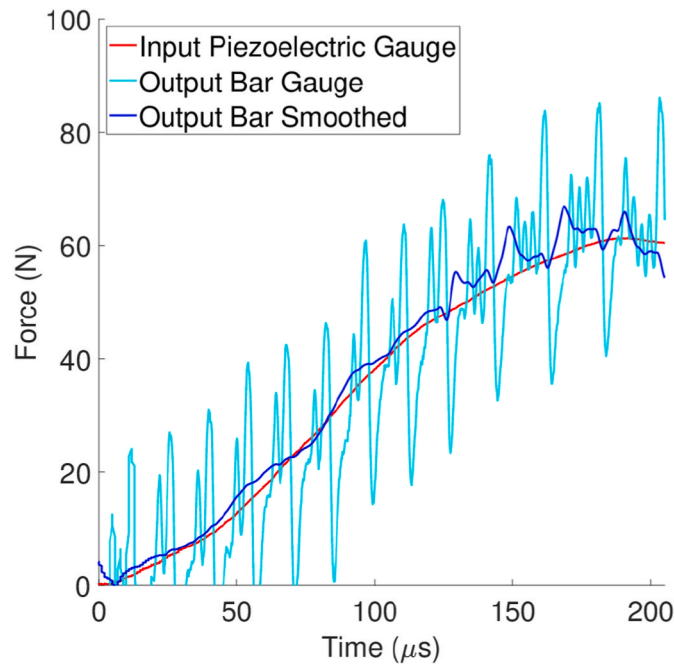


Fig. 39. Comparison of data from the piezoelectric gauge at the input-bar specimen interface, and the surface-mounted gauge on the output bar, demonstrating the considerable improvement in data quality from the piezoelectric gauge, and that the specimen is in static equilibrium during the experiment.

A.5. Interrupted experiments: data

Results for the interrupted experiments are plotted in Fig. 40a. There is hardly any strain activated damage (or indeed, modulus enhancement) for the 5% F-NRs as their curves lay on top of those for the U-NR (allowing for experimental variation). For this reason, the 50% F-NRs are focused on and are shown separately in Fig. 40b for clarity.

To allow the temperature dependence of the damage for the 50% F-NRs to be investigated, further experiments were performed at -40 and -50 °C. These temperatures were selected as in §4.2, it was shown that these are the temperatures where the mechanical response transitions from rubbery to leathery. These results are shown in Figure 41.

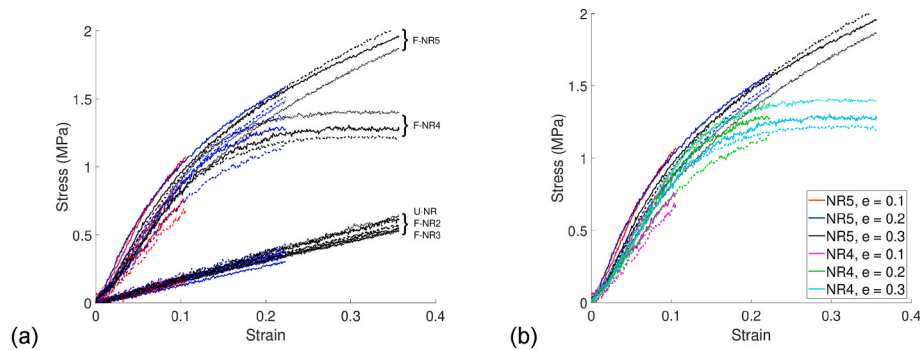


Fig. 40. Results of varying strain quasi-static compression experiments at 10^{-2} s^{-1} and 25 °C for (a) all grades of rubber and (b) only 50% F-NRs to focus on strain activated damage.

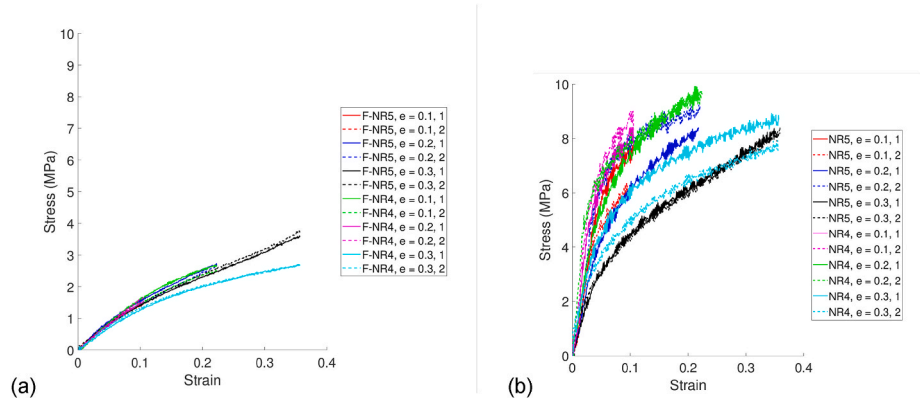


Fig. 41. Results of varying strain quasi-static compression experiments at 10^{-2} s^{-1} for 50% F-NRs at (a) -40 °C and (b) -50 °C.

A.6. Photographs highlighting damage

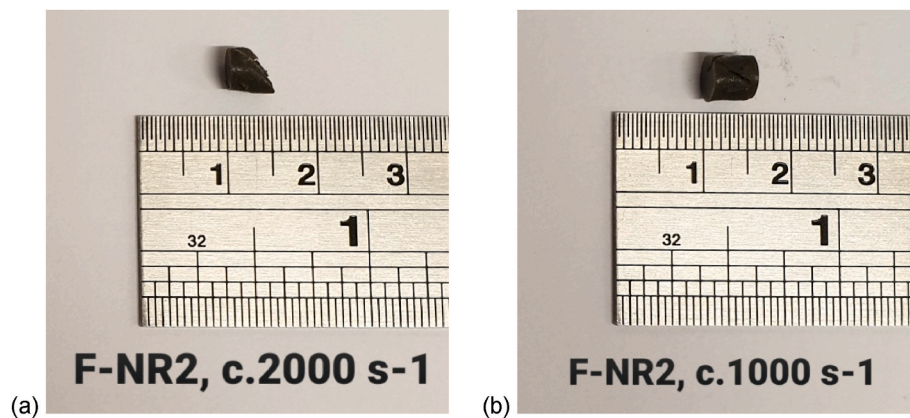


Fig. 42. Post-mortem examination for high strain rate experiments at $-60\text{ }^{\circ}\text{C}$ for F-NR2 at (a) c. 1000 s^{-1} and (b) c. 2000 s^{-1} .

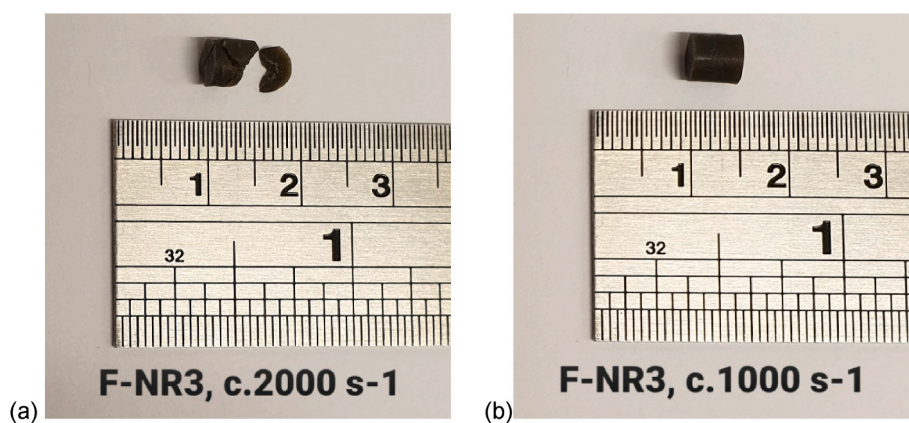


Fig. 43. Post-mortem examination for high strain rate experiments at $-60\text{ }^{\circ}\text{C}$ for F-NR3 at (a) c. 1000 s^{-1} and (b) c. 2000 s^{-1} .

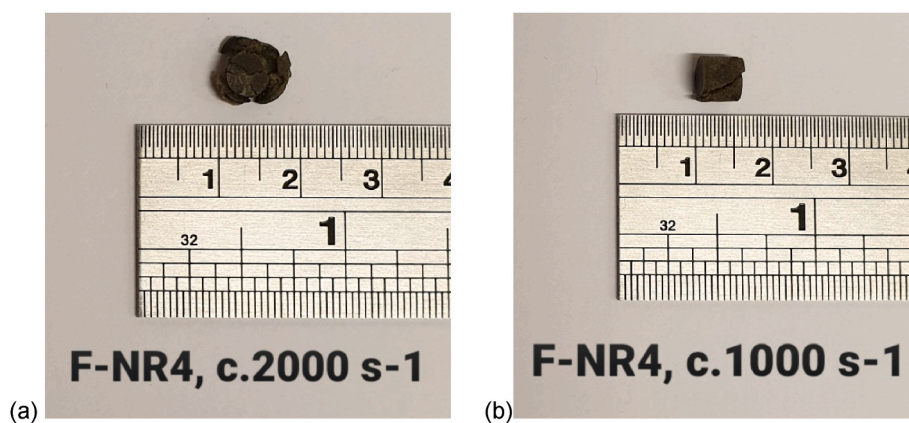


Fig. 44. Post-mortem examination for high strain rate experiments at $-60\text{ }^{\circ}\text{C}$ for F-NR4 at (a) c. 1000 s^{-1} and (b) c. 2000 s^{-1} .



Fig. 45. Post-mortem examination for high strain rate experiments at $T \approx -55^\circ\text{C}$ for F-NR5 at c. 1000 s^{-1} .

A.7. Eyring plots

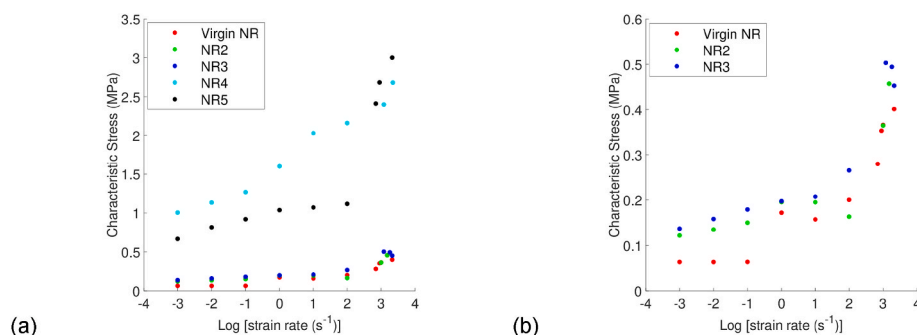


Fig. 46. Eyring plots showing 'characteristic' stress vs strain rate at 25°C for (a) all the materials and (b) the three weaker materials.

References

- [1] D.M. Williamson, C.R. Siviour, W.G. Proud, S.J.P. Palmer, R. Govier, K. Ellis, P. Blackwell, C. Leppard, Temperature-time response of a polymer bonded explosive in compression (EDC37), *J. Phys. Appl. Phys.* 41 (2008), 085404.
- [2] D.R. Drodge, D.M. Williamson, S.J.P. Palmer, W.G. Proud, R.K. Govier, The mechanical response of a PBX and binder: combining results across the strain-rate and frequency domains, *J. Phys. Appl. Phys.* 43 (2010), 335403.
- [3] C. Siviour, P. Laity, W. Proud, J. Field, D. Porter, P. Church, P. Gould, W. Huntingdon-Thresher, High strain rate properties of a polymer-bonded sugar: their dependence on applied and internal constraints, *Proc. Math. Phys. Eng. Sci.* 464 (2008) 1229–1255.
- [4] M.J. Kendall, C.R. Siviour, Experimentally simulating high rate composite deformation in tension and compression: polymer bonded explosive simulant, *Journal of Dynamic Behavior of Materials* 1 (2015) 114–123.
- [5] F.S. Conant, G.L. Hall, W.J. Lyons, Equivalent effects of time and temperature in the shear creep and recovery of elastomers, *J. Appl. Phys.* 21 (1950) 499–504.
- [6] C. Bauwens-Crowet, The compression yield behaviour of polymethyl methacrylate over a wide range of temperatures and strain-rates, *J. Mater. Sci.* 8 (1973) 968–979.
- [7] J.L. Jordan, J.E. Spowart, M.J. Kendall, B. Woodworth, C.R. Siviour, Mechanics of particulate composites with glassy polymer binders in compression, *Philosophical transactions. Series A, Mathematical, physical, and engineering sciences* 372 (2014), 20130215.
- [8] C. Bauwens-Crowet, J.C. Bauwens, G. Homès, Tensile yield-Stress behavior of glassy polymers, *J. Polym. Sci.* 7 (1969) 735–742.
- [9] J.L. Jordan, C.R. Siviour, B.T. Woodworth, High strain rate tensile and compressive effects in glassy polymers, *EPJ Web Conf.* 26 (2012) 1001.
- [10] C. Siviour, S. Walley, W. Proud, J. Field, The high strain rate compressive behaviour of polycarbonate and polyvinylidene difluoride, *Polymer* 46 (2005) 12546–12555.
- [11] H. Kolsky, An investigation of the mechanical properties of materials at very high rates of loading, *Proc. Phys. Soc. B* 62 (1949) 676.
- [12] W. Chen, B. Song, Split Hopkinson (Kolsky) Bar, *Mechanical Engineering Series*, Springer US, Boston, MA, 2011.
- [13] G.T. Gray, W.R. Blumenthal, Split-hopkinson pressure bar testing of soft materials, in: *ASM Handbook Volume 8, Mechanical Testing and Evaluation*, ASM International, 2000, pp. 488–496.
- [14] W. Chen, B. Zhang, M.J. Forrestal, A split Hopkinson bar technique for low impedance materials, *Exp. Mech.* 39 (1999) 81–85.
- [15] M.J. Kendall, D.R. Drodge, R.F. Froud, C.R. Siviour, Stress gage system for measuring very soft materials under high rates of deformation, *Meas. Sci. Technol.* 25 (2014), 075603.
- [16] F. Pierron, H. Zhu, C. Siviour, Beyond Hopkinson's bar, *Phil. Trans. Math. Phys. Eng. Sci.* 372 (2014), 20130195.
- [17] M.J. Kendall, C.R. Siviour, Experimentally simulating adiabatic conditions: approximating high rate polymer behavior using low rate experiments with temperature profiles, *Polymer* 54 (2013) 5058–5063.

- [18] M.J. Kendall, C.R. Siviour, Experimentally simulating high-rate behaviour: rate and temperature effects in polycarbonate and PMMA, *Philosophical transactions. Series A, Mathematical, Physical, and Engineering Sciences* 372 (2014), 20130202.
- [19] A.R. Trivedi, C.R. Siviour, A novel methodology for predicting the high rate mechanical response of polymers from low rate data: application to (plasticised) poly(vinyl chloride), *Mech. Time-Dependent Mater.* (2020) 1–27.
- [20] A.R. Trivedi, C.R. Siviour, A simple rate-temperature dependent hyperelastic model applied to neoprene rubber, *Journal of Dynamic Behavior of Materials* 6 (2020) 336–347.
- [21] M.J. Kendall, C.R. Siviour, Rate dependence of poly(vinyl chloride), the effects of plasticizer and time-temperature superposition, *Proceedings of the Royal Society A: Mathematical, Physical and Engineering Sciences* 470 (2014), 20140012–20140012.
- [22] Mrpra, Natural Rubber Engineering Data Sheet - EDS 19, Malaysian Rubber Producers' Research Association, 1980. Technical Report.
- [23] D.A. Gorham, The effect of specimen dimensions on high strain rate compression measurements of copper, *J. Phys. Appl. Phys.* 24 (1991) 1489–1492.
- [24] L.C. Thomas, Modulated DSC Basics; Optimization of MDSC Experimental Conditions, Technical Report, 2011.
- [25] H.K. Frensdorff, The thermal diffusivity of natural rubber, *J. Appl. Polym. Sci.* 6 (1962). S28–S29.
- [26] C.A. Rezende, F.C. Bragança, T.R. Doi, L.T. Lee, F. Galembeck, F. Boué, Natural rubber-clay nanocomposites: mechanical and structural properties, *Polymer* 51 (2010) 3644–3652.
- [27] G.P. Baeza, C. Dessi, S. Costanzo, D. Zhao, S. Gong, A. Alegria, R.H. Colby, M. Rubinstein, D. Vlassopoulos, S.K. Kumar, Network dynamics in nanofilled polymers, *Nat. Commun.* 7 (2016), 11368.
- [28] Q. Chen, S. Gong, J. Moll, D. Zhao, S.K. Kumar, R.H. Colby, Mechanical reinforcement of polymer nanocomposites from percolation of a nanoparticle network, *ACS Macro Lett.* 4 (2015) 398–402.
- [29] H. Eyring, Viscosity, plasticity, and diffusion as examples of absolute reaction rates, *J. Chem. Phys.* 4 (1936) 283–291.
- [30] M.L. Williams, R.F. Landel, J.D. Ferry, The temperature dependence of relaxation mechanisms in amorphous polymers and other glass-forming liquids, *J. Am. Chem. Soc.* 77 (1955) 3701–3707.
- [31] G.T. Gray III, W.R. Blumenthal, Split-hopkinson pressure bar testing of soft materials, in: *ASM Handbook Volume 8, Mechanical Testing and Evaluation*, ASM International, 2000, pp. 488–496.
- [32] C.K. Dharan, F.E. Hauser, Determination of stress-strain characteristics at very high strain rates, *Exp. Mech.* 10 (1970) 370–376.
- [33] D.A. Gorham, P.H. Pope, J. Field, An improved method for compressive stress-strain measurements at very high strain rates, *Proc. Roy. Soc. Lond. Math. Phys. Sci.* 438 (1992) 153–170.
- [34] A. Trautmann, C.R. Siviour, S.M. Walley, J.E. Field, Lubrication of polycarbonate at cryogenic temperatures in the split Hopkinson pressure bar, *Int. J. Impact Eng.* 31 (2005) 523–544.
- [35] T. Goudarzi, D.W. Spring, G.H. Paulino, O. Lopez-Pamies, Filled elastomers: a theory of filler reinforcement based on hydrodynamic and interphasial effects, *J. Mech. Phys. Solid.* 80 (2015) 37–67.
- [36] S. Ravindran, A. Tessema, A. Kidane, Local deformation and failure mechanisms of polymer bonded energetic materials subjected to high strain rate loading, *Journal of Dynamic Behavior of Materials* 2 (2016) 146–156.
- [37] D.R. Drodge, D.M. Williamson, Understanding damage in polymer-bonded explosive composites, *J. Mater. Sci.* 51 (2016) 668–679.
- [38] N. Fleck, Adiabatic shear instability: theory, in: *Mechanical Properties and Testing of Polymers*, Springer, 1999, pp. 15–19.
- [39] Y.L. Bai, Thermo-plastic instability in simple shear, *J. Mech. Phys. Solid.* 30 (1982) 195–207.
- [40] N.A. Fleck, W.J. Stronge, J.H. Liu, High strain-rate shear response of polycarbonate and polymethyl methacrylate, *Proceedings of the Royal Society of London. A. Mathematical and Physical Sciences* 429 (1990) 459–479.
- [41] J. Richeton, S. Ahzi, L. Daridon, Y. Rémond, A formulation of the cooperative model for the yield stress of amorphous polymers for a wide range of strain rates and temperatures, *Polymer* 46 (2005) 6035–6043.
- [42] K. Cao, Y. Wang, Y. Wang, Effects of strain rate and temperature on the tension behavior of polycarbonate, *Mater. Des.* 38 (2012) 53–58.
- [43] J. Eshelby, The determination of the elastic field of an ellipsoidal inclusion, and related problems, *Proc. Roy. Soc. Lond. Math. Phys. Sci.* 241 (1957) 376–396.
- [44] R. Hill, Elastic properties of reinforced solids: some theoretical principles, *J. Mech. Phys. Solid.* 11 (1963) 357–372.
- [45] T.B. Lewis, L.E. Nielsen, Dynamic mechanical properties of particulate-filled composites, *J. Appl. Polym. Sci.* 14 (1970) 1449–1471.
- [46] T. Mori, K. Tanaka, Average stress in matrix and average elastic energy of materials with misfitting inclusions, *Acta Metall.* 21 (1973) 571–574.
- [47] E. Guth, Theory of filler reinforcement, *J. Appl. Phys.* 16 (1945) 20–25.
- [48] H.M. Smallwood, Limiting law of the reinforcement of rubber, *J. Appl. Phys.* 15 (1944) 758–766.
- [49] J.S. Bergström, M.C. Boyce, Mechanical behavior of particle filled elastomers, *Rubber Chem. Technol.* 72 (1999) 633–656.